

## RESEARCH ARTICLE

10.1029/2018JC014866

## Key Points:

- Upper global ocean mode water are the hot spots of 2006–2015 ocean heat trend
- Southern Hemisphere mode water gained volume and buoyancy over 2006–2015
- Wind forcing and oceanic adjustment may partly explain the interannual mode water volume change

## Correspondence to:

N. Kolodziejczyk,  
nicolas.kolodziejczyk@univ-brest.fr

## Citation:

Kolodziejczyk, N., Llovel, W., & Portela, E. (2019). Interannual variability of upper ocean water masses as inferred from Argo Array. *Journal of Geophysical Research: Oceans*, 124, 6067–6085. <https://doi.org/10.1029/2018JC014866>

Received 14 DEC 2018

Accepted 31 JUL 2019

Accepted article online 6 AUG 2019

Published online 23 AUG 2019

# Interannual Variability of Upper Ocean Water Masses as Inferred From Argo Array

Nicolas Kolodziejczyk<sup>1</sup> , William Llovel<sup>2</sup> , and Esther Portela<sup>1</sup>

<sup>1</sup>University of Brest, CNRS, IRD, Ifremer, Laboratoire d'Océanographie Physique et Spatiale, Plouzané, France, <sup>2</sup>LEGOS, CNRS/IRD/CNES/UPS, Toulouse, France

**Abstract** Interannual variability of Ocean Heat Content (OHC) is intimately linked to ocean water mass changes. Water mass characteristics are imprinted at the ocean surface and are modulated by climate variability on interannual to decadal time scales. In this study, we investigate the water mass change and their variability using an isopycnal decomposition of the OHC. For that purpose, we address the thickness and temperature changes of these water masses using both individual temperature-salinity profiles and optimal interpolated products from Argo data. Isopycnal decomposition allows us to characterize the water mass interannual variability and decadal trends of volume and OHC. During the last decade (2006–2015), much of interannual and decadal warming is associated with Southern Hemisphere Subtropical Mode Water and Subantarctic Mode Water, particularly in the South Pacific Eastern Subtropical Mode Water, the Southeastern Indian Subantarctic Mode Water, and the Southern Pacific Subantarctic Mode Water. In contrast, Antarctic Intermediate Water in the Southern Hemisphere and North Atlantic Subtropical Mode Water in the Northern Hemisphere have cooled. This OHC interannual variability is mainly explained by volume (or mass) changes of water masses related to the isopycnal heaving. The forcing mechanisms and interior dynamics of water masses are discussed in the context of the wind stress change and ocean adjustment occurring at interannual time scale.

## 1. Introduction

Interannual variability of Ocean Heat Content (OHC) is intimately linked to ocean water mass changes. Water mass characteristics are imprinted in terms of physical and biogeochemical properties at the ocean surface by the climate natural variability on interannual to decadal time scales. Since the 1970s, the global ocean has stored more than 90% of the planetary warming caused by global energy imbalance (IPCC, 2013; von Schuckmann et al., 2016), and it has stored about 25% of the anthropogenic CO<sub>2</sub> emissions (Fine et al., 2017; Sallée et al., 2013). Thus, the knowledge about water mass formation and their variability is fundamental to improve our understanding of the mechanisms driving the heat, freshwater, biogeochemical tracers, and carbon sequestration processes in the global ocean interior.

Before the 2000s, in situ observations of temperature of the water column were spatially and temporally sparse (Abraham et al., 2013) and OHC change estimates were largely underestimated and biased toward the better sampled Northern Hemisphere, particularly the North Atlantic (Durack et al., 2014). Since the early 2000s, the Argo program has provided high-quality 0–2,000-m temperature/salinity profiles over the global ocean (Gould et al., 2004). The Argo network provides the first homogeneous global coverage of upper ocean profiles, which has significantly reduced uncertainties about rates of global ocean warming over the past decade (Figure 1).

Additionally, the recent ocean warming trend has been mainly explained by warming located within the upper ocean layer (above 2,000 m) of the water column at subtropical/midlatitudes of the Southern Hemisphere, more precisely within southeastern Indian and southern Pacific Ocean subtropical gyres (Figures 1c and 1d; e.g., Desbruyères et al., 2017; Gao et al., 2017; Häkkinen et al., 2015, 2016; Llovel & Terray, 2016; Roemmich et al., 2015; Wijffels et al., 2016).

Subtropical and Subpolar ocean of the Southern Hemisphere is populated by Mode Water (ST/SAMW). Extensively documented in the literature, Mode Waters (MW) have been defined by their relatively uniform properties over a large volume in the ocean (e.g., Hanawa & Tally, 2001; Speer and Forget et al., 2011). MW are formed by winter buoyancy loss driving convection. They are thus temporarily isolated from the surface

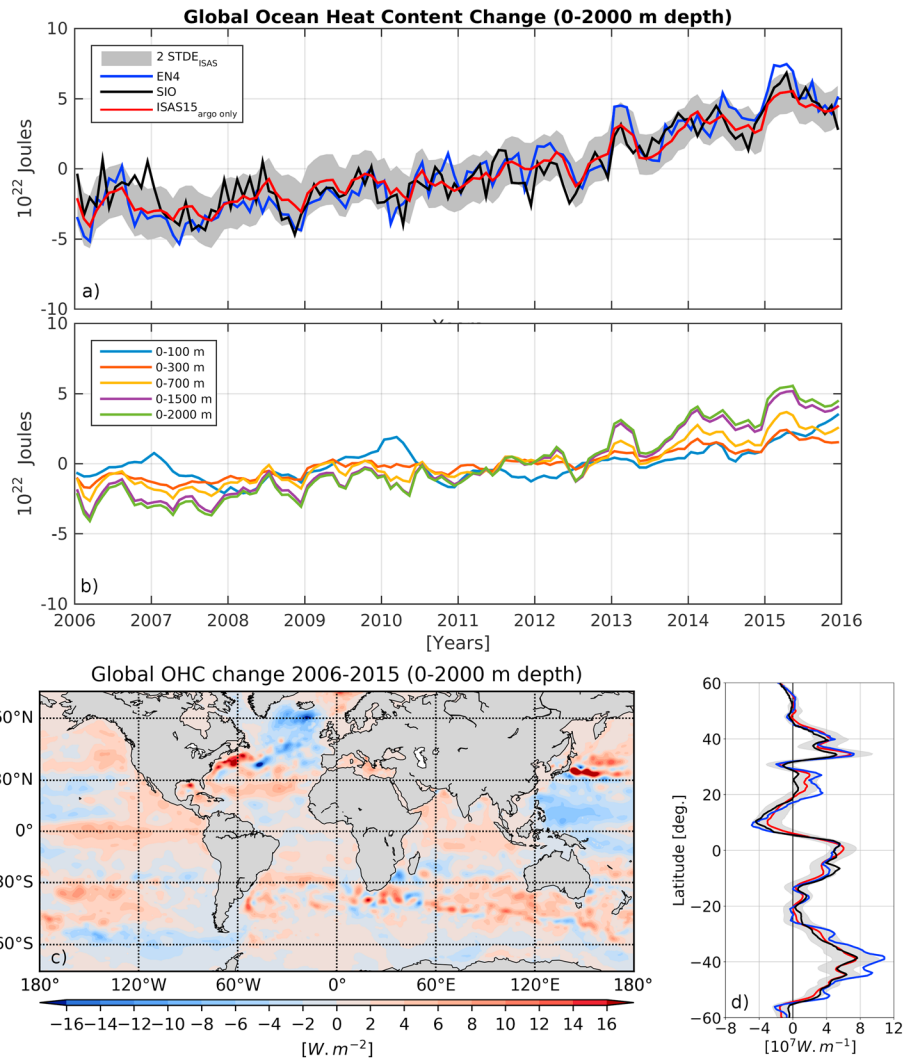


**Figure 1.** (a) The 0–2,000-m depth Global Ocean Heat Content Change (in J) using ISAS15 (red), Roemmich and Gilson SIO (black), EN4 (blue) along with error bar ( $2\epsilon$ ) computed on ISAS15. (b) Depth-layer contribution to the Global Heat Content Change in depth ranges 0–100 m (blue), 0–300 m (red), 0–700 m (yellow), 0–1,500 m (purple), and 0–2,000 m (green) depth from ISAS15. (c) The 0–2,000-m depth OHC trend over the period 2006–2015 (in  $W/m^2$ ) from ISAS15. (d) Zonal integrated 0–2,000-m depth OHC trend over the period 2006–2015 (in  $W/m$ ) from ISAS15 (red), SIO (black), and EN4 (blue).

by the seasonal thermocline and characterized by their relative low potential vorticity, that is, low stratification. Subtropical Mode Water (STMWs) and Subpolar MWs are found the upper ocean subtropical and subpolar gyre, respectively. For example, the North Atlantic STMW (NASTMW; Worthington, 1959; Maze & Marshall, 2011) lays between the  $\sigma_\theta = 26.4\text{--}26.6 \text{ kg/m}^3$  isopycnals and it is the largest subtropical MW pool in the Northern Hemisphere, while Sub-Antarctic Mode Waters (SAMW; McCartney, 1977, 1982), encompassing the  $\sigma_\theta = 26.7\text{--}27.0 \text{ kg/m}^3$  isopycnal surfaces, constitute the largest pool of upper ocean MW in the Southern Hemisphere.

Although, the water mass properties (T/S) of upper ocean MW are remarkably stable over time (Forget et al., 2011; Speer & Forget, 2013), recent studies (e.g., Desbruyères et al., 2017; Häkkinen et al., 2015, 2016), using a heave/spice decomposition, pointed out that the recent upper warming trend is explained by a deepening of lighter subtropical isopycnal surfaces (heave) rather than by the temperature change along the isopycnal surfaces. The heaving trends exhibit different patterns depending on the considered time scale, over 20–50 years (Häkkinen et al., 2015, 2016) and over 10 years (Desbruyères et al., 2017). These studies only diagnosed long-

term trends (>10 years) from large-scale basin patterns and they did not focus on specific water masses, location, and warming mechanisms. More recently, using the thermostatic and halostatic approach to define SAMW (Hanawa & Tally, 2001), Gao et al. (2017) found a good correlation between the recent OHC and volume decadal trends (2005–2015) of SAMW. However, this approach focused on SAMW only, and it does not detail the specific hot spots of water mass subduction and interior change which are known to be important for the larger-scale ocean variability (Rintoul, 2018; Sallée et al., 2010). In contrast, Evans et al. (2017) recently showed the importance of interannual wind forcing for explaining year to year variability of the NATSTMW and associated OHC. Less attention has been paid on diagnosing the interannual variability of ocean water masses and its contribution to OHC changes. Therefore, the present study tends to better ascertain this contribution.

Argo sampling has made possible to estimate more precisely the seasonal to interannual variability of large-scale thermohaline isopycnal changes at regional scales. These changes are associated with spiciness, as defined by McDougall and Kzysik (2015) and their dissemination within the upper ocean (e.g., Kolodziejczyk et al., 2014; Kolodziejczyk & Gaillard, 2012; Sasaki et al., 2010; Schneider, 2000; Schneider et al., 1999). A consistent record of both temperature and salinity profiles provides a better understanding of the ocean thermohaline variability in an isopycnal framework. The isopycnal layers are connected to the surface where water masses are transformed by heat and freshwater fluxes, that is, air-sea buoyancy fluxes. Cross-isopycnal mixing processes, wind stress curl, and advection also control the volume and interior ocean path of the isopycnal layers (e.g., Downes et al., 2011; Luyten et al., 1983; Speer & Forget, 2013; Speer & Tzipermann, 1992; Tzipermann, 1986; Walin, 1982). At the interannual time scale, besides the importance of mixing processes in the interior of the oceans, questions remain on the mechanisms related to the isopycnal heaving and passive tracer mode following the subduction of water masses along isopycnal surfaces (Liu, 1999; Liu & Shin, 1999). Both heave/spice decomposition and T-S volumetric approaches (e.g., Zika et al., 2009; Döös et al., 2012; Speer & Forget, 2013; Evans et al., 2014, 2017) provide a different perspective and new insights in both characteristics and variability of ocean water masses. The question of water mass variability from in situ measurements is rarely tackled in the literature (especially because observational time series were scarce before 2000s). Therefore, in this study, using the global Argo profile data set, we adopt an isopycnal decomposition of the integral of OHC, volume, and temperature to characterize the interannual variability of the upper ocean water masses and to infer the driving mechanisms

The questions addressed in this study are the following: (i) where the water mass hot spots of OHC variability are located over the last decade? and (ii) which forcing and interior dynamics driving water mass variability can be inferred from the Argo data set? The remainder of this paper is organized as follows: the data and method will be presented in the next section. Then, the isopycnal OHC, thickness, and temperature trends over the 2006–2015 period are documented. The forcing and ocean interior dynamics at the hot spots of water mass interannual variability will be investigated. Finally, we will discuss the results and end with some concluding remarks on the study.

## 2. Data and Method

### 2.1. In Situ Temperature and Salinity Data

We consider the monthly gridded fields of temperature and salinity obtained from “In Situ Analysis System” (ISAS), an optimal interpolation (Bretherton et al., 1976) tool specifically designed for synthesis of the Argo global data set (Gaillard et al., 2009, 2016). We consider the latest version named ISAS15, which considers only the delayed mode of Argo data over the period 2002–2015 (Kolodziejczyk et al., 2017). Although the Argo array started in early 2000 ([www.argo.net](http://www.argo.net)), nominal global sampling has only been reached since 2006. We thus decided to focus our study over the period 2006–2015 (10 years). The gridded fields were produced over the global ocean by the Argo-France project with data sets downloaded from the Coriolis Global Data Center. The ISAS data set preprocessing includes a climatological test applied to the data set, followed by visual checking of any suspicious profiles. The temperature and salinity fields are vertically interpolated on 152 depth levels ranging from 0- to 2,000-m depth (5- to 10-m resolution within the shallowest 500-m depth and 20-m resolution below), on a half-degree isotropic horizontal grid. However, ISAS15 effective resolution is set by two correlation spatial scales: a large spatial scale of 300 km and a small spatial scale

of the order of the first deformation radius with a latitudinal dependency and a zonal elongation (600 km) at the equator. This particular ISAS15 analysis differs slightly from the product presented by Gaillard et al. (2016) in two respects: the reference climatology and the optimal interpolation parameters. While Gaillard et al. (2016) used reference climatology based on ISAS11 analysis (2004–2010), we used the average of ISAS13, based on the period 2004–2012.

The second product used in this study is the version 4 of the objective analyses from the Met Office Hadley Centre of global ocean temperature and salinity in situ profiles, named EN4 (Good et al., 2013). The data set used in EN4, including not only Argo data but also other in situ measurements, followed several quality controls described in Good et al. (2013). The EN4 analysis is a monthly gridded product on 46 depth levels over the full water column and 1° horizontal grid. Two isotropic horizontal covariance scales are applied in this gridded products being 300 and 400 km. In the tropics, an anisotropic zonal 1,500-km scale is used. Two vertical correlation scales of 200 and 100 m are also introduced. Contrary to ISAS, the first guess of analyses is determined by monthly climatology for the period 1971–2000 plus a weighted analyzed anomaly from the previous calendar month. The EN4 product covers the period 1900 to present, but only the 2006–2015 period is considered.

The third product used in this study is the Scripps Institution of Oceanographic product based on optimal interpolation of Argo temperature and salinity profiles (Roemmich & Gilson, 2009). The Scripps Institution of Oceanographic product was interpolated on 56 pressure standard levels and a 1° regular grid between 60°S and 60°N. Two horizontal covariance scales are chosen for the Scripps Institution of Oceanographic optimal interpolation. A long covariance scale of 1,111 km accounting for 23% of the total variance is used during the first interpolation. Then this first analysis is used as a first guess in a second interpolation using a shorter covariance scale of 140 km chosen to account for about 77% of the total variance.

In order to check the consistency of the results from  $z$ -level standardized OI fields we computed the trend over 2006–2015 of isopycnal OHC, thickness, and temperature from individual delayed mode Argo profiles in 3° × 3° boxes (which is the nominal target coverage of Argo network) and for each potential density layers of resolution  $\Delta\sigma_\theta = 0.1 \text{ kg/m}^3$ .

## 2.2. Wind Stress Data From Atmospheric Reanalysis

A monthly gridded zonal and meridional wind stress product with a horizontal resolution of 1.58° × 1.58° was obtained from the National Center for Environment and Prediction Reanalysis-2 ([www.esrl.noaa.gov/psd/data/gridded/data.ncep.reanalysis.html](http://www.esrl.noaa.gov/psd/data/gridded/data.ncep.reanalysis.html)). We computed the monthly wind stress curl over the global ocean between 2016 and 2015. We also used monthly averaged 0.758° × 0.758° gridded wind fields between 2006 and 2015 from the European Reanalysis and Assimilation-Interim reanalysis provided by the European Center for Medium-Range Weather Forecasts ([www.ecmwf.int/en/research/climate-reanalysis/era-interim](http://www.ecmwf.int/en/research/climate-reanalysis/era-interim)).

## 2.3. Isopycnal Heat Content, Thickness, and Temperature Computation

For the purposes of this study, OHC, thickness, and temperature for each isopycnal layer were computed as follows:

$$OHC_{12} = \int_{z_1}^{z_2} \rho C_p T(z) dz \quad (1.1)$$

$$h_{12} = \int_{z_1}^{z_2} dz \quad (1.2)$$

$$T_{12} = \frac{1}{h_{12}} \int_{z_1}^{z_2} T(z) dz \quad (1.3)$$

where  $\rho$  is the seawater density,  $C_p$  is the isobaric thermal capacity of seawater,  $T$  is the potential temperature anomaly with respect to 0 °C, and  $z_1$  and  $z_2$  are the depth of the lower and upper isopycnal surfaces, respectively. Isopycnal layers have a regular spacing of  $\Delta\sigma_\theta = 0.1 \text{ kg/m}^3$ , spanning between  $24 < \sigma_\theta < 28 \text{ kg/m}^3$ . The upper layer between the surface and  $\sigma_\theta = 24 \text{ kg/m}^3$ , which encompasses mainly tropical water masses, are treated as a single layer.

In this study, the interannual variability of the different parameters is computed as the interannual anomalies, that is, removing the monthly climatology computed over the period 2006–2015 from the monthly time series. Then, from the interannual anomalies time series, the linear 2006–2015 trend, if significant, is extracted. This linear trend may explain a given percentage of the interannual variance. The 2006–2015 trend contribution to the interannual variance will be discussed in this study.

#### 2.4. Mixed Layer Depth Data

The mixed layer depth (MLD) has been computed from ISAS15 fields with a density criterion of  $\Delta\sigma_\theta = 0.03 \text{ kg/m}^3$  from the 10-m depth value of density following de Boyer Montégut et al. (2004). This MLD computed from OI smoothed field have been compared with  $1^\circ \times 1^\circ$  binned MLD climatology computed from individual Argo profile (de Boyer Montégut et al., 2004). The ISAS MLD slightly overestimates the MLD in the Southern Ocean, but the agreement remains reasonable over the global ocean.

#### 2.5. Geostrophic Velocity

The mean Montgomery potential and geostrophic velocities were computed following McDougall and Klocker (2010) (based on the GSW V3.0 library, TEOS-10) using the mean ISAS15 hydrological data. The reference level for mean geostrophic velocities between 2006 and 2015 was the average of the map of absolute surface dynamic topography from AVISO satellite altimetry products computed from sea level anomaly and mean absolute dynamic topography, named MDT\_CNES-CLS13, based on Gravity Recovery and Climate Experiment, satellite altimetry, and in situ measurement (Rio et al., 2011).

Since ISAS15 reaches only 2,000-m depth, the mean barotropic component of the current velocity over the full depth water column was derived using World Ocean Atlas 2009 (providing surface to 5,500-m depth hydrological data) by Pr. Colin de Verdière as follow: Ollitrault and Colin de Verdière (2014) obtained the absolute geopotential from the mean Argo float displacement at 1,000-m depth. The World Ocean Atlas 2009 was used to obtain the geopotential relative to 1,000-m depth. Adding the two together gives an absolute geopotential at all depths from which three-dimensional absolute geostrophic velocities. Averaging vertically from surface to bottom gives the barotropic current velocities.

### 3. Results

#### 3.1. Decadal Trends

Over the last decade, global ocean heat content (0–2,000 m) has increased by about  $8 \times 10^{22} \text{ J}$  (Figure 1a). Since 2006, Argo interpolated T/S fields have confirmed the unabated global mean OHC increase in the upper 2,000 m of the ocean between 2005 and 2014 (Roemmich et al., 2015; Wijffels et al., 2016). The upper layer between 0- and 700-m depth has contributed significantly, accounting for about half of the global warming (about  $5 \times 10^{22} \text{ J}$ ; Figure 1b) while the deepest layer (between 700 and 2,000 m) contributed to an increase of less than  $4 \times 10^{22} \text{ J}$  (Figure 1b). The global map of the 0–2,000-m depth OHC trend (Figure 1c) shows that Southern Hemisphere subtropical basins and tropical Indian Ocean have positive OHC trends ( $+2 \text{ W/m}^2$ ), while subpolar North Atlantic and subtropical North Pacific have lost heat ( $-4 \text{ W/m}^2$ ). This shows that the regions of decreasing/increasing OHC are mainly located in Northern/Southern Hemisphere. The zonal integration (Figure 1d) shows strong ocean warming (up to  $5 \times 10^7 \text{ W/m}$ ) occurring in the tropics while the most striking feature is concentration of most of the warming in the Southern Hemisphere ( $7 \times 10^7 \text{ W/m}$ ; Figure 1d), in line with Roemmich et al. (2015). To understand individual basin and water mass contributions year by year, specific regional and full-depth investigation are needed.

The interannual variability of isopycnal layer thickness (volume) have been computed removing the monthly climatology over the period 2006–2015 from every individual monthly field (Figure 2). Figures 2d–2f show that the variability is mainly located in the MW and intermediate waters, that is, around the density layer of  $\sigma_\theta = 25\text{--}26 \text{ kg/m}^3$  and  $\sigma_\theta = 26.8\text{--}27.3 \text{ kg/m}^3$  in the Southern Hemisphere and around  $\sigma_\theta = 26.0\text{--}26.5 \text{ kg/m}^3$  and  $\sigma_\theta = 27.0\text{--}27.7 \text{ kg/m}^3$  in the Northern Hemisphere (Figures 2d–2f).

In order to quantify the OHC change over the 2006–2015 period for each density and oceanic basin, we have computed the interannual STD (gray in Figures 3a, 3c, 3e, 3g, and 3i) of OHC. We have overlaid the part of the STD explained by the 2006–2015 trend alone (reds in Figures 3a, 3c, 3e, 3g, and 3i) for individual isopycnal layers within all the ocean basins and the three different products. The 10-year trend computed from

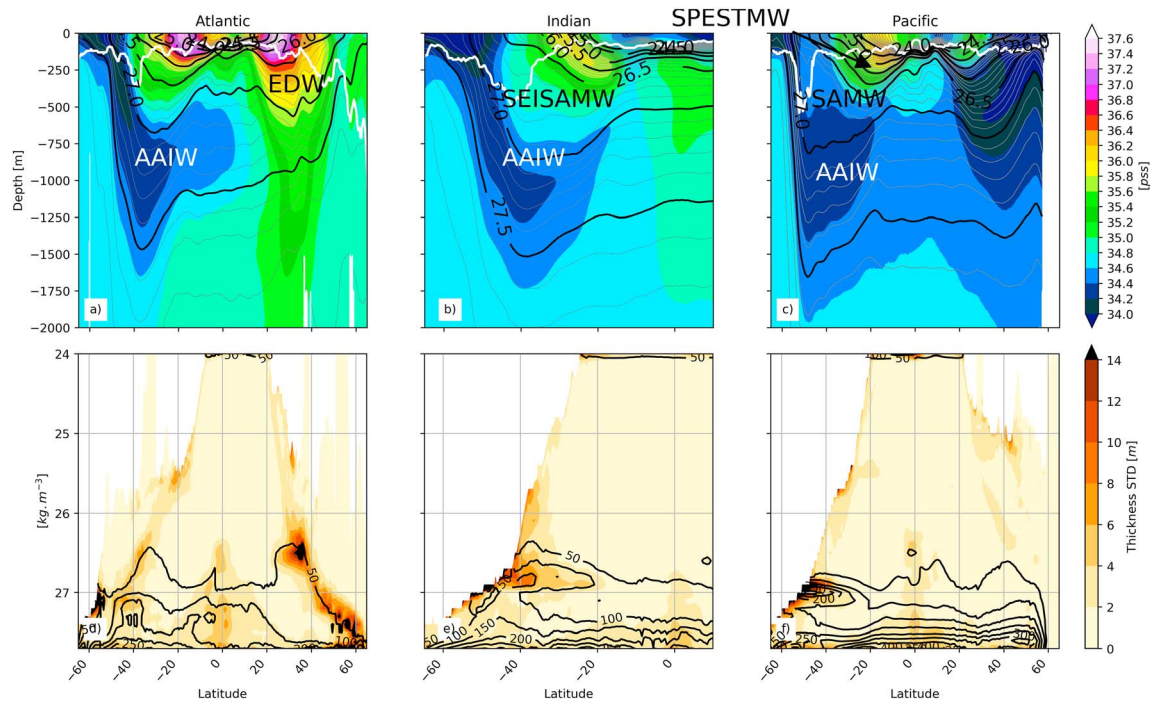


**Figure 2.** Latitude–depth section of salinity (color shading; in pss) and  $\sigma_\theta$  potential density anomaly (black thick and gray thin contours; in  $\text{kg}/\text{m}^3$ ) at (a)  $32.5^\circ\text{W}$  across the Atlantic Ocean, (b)  $90^\circ\text{E}$  across the Indian Ocean, and (c)  $-150^\circ\text{W}$  across the Pacific Ocean computed from ISAS15. South Pacific Eastern Subtropical Mode Water (SPEATMW); Subantarctic Mode Water (SAMW); South Eastern Indian Subantarctic Mode Water (SEISAMW), Eighteen Degree Water (EDW), and Antarctic Intermediate Water (AAIW) are labeled (see Hanawa & Tally, 2001) White contour is the deepest winter mixed layer over the 2006–2015 period. (d) Atlantic:  $80^\circ\text{W}$ – $0^\circ\text{E}$ , (e) Indian:  $20^\circ$ – $150^\circ\text{E}$ , and (f) Pacific:  $150^\circ$ – $90^\circ\text{W}$  zonal average of isopycnal layer thickness computed from ISAS15 (black contours; CI: 50 m) and STD (colors; CI: 2 m).

each product is shown in Figures 3b, 3d, 3f, 3h, and 3j. The three products present consistent isopycnal layer OHC interannual STD (gray; Figures 3a, 3c, 3e, 3g, and 3i) and decadal trends (red/blue Figure 3). The STD and trends located at densities larger than  $\sigma_\theta = 27.5 \text{ kg}/\text{m}^3$  will be not discussed because they are not full sampled within the 2,000-m-depth Argo profiles (see Figure 2a).

In the North Atlantic Ocean, the distribution of the OHC change reveals strong interannual variability of OHC for the  $\sigma_\theta = 26.4$ – $26.5 \text{ kg}/\text{m}^3$  isopycnal layer (Figure 3a), which is mainly associated with the core of North Atlantic STMW. In this class of water masses, the 10-year trend leads to a divergence of heat of about than  $1.8 \times 10^{22} \text{ J}$  (Figures 2a and 3b) which has been explained by the adjustment of the subtropical gyre under interannual wind stress curl change (Evans et al., 2017). For the South Atlantic Ocean about  $1.5 \times 10^{22} \text{ J}$  were converging in the  $\sigma_\theta = 26.0$ – $27.0 \text{ kg}/\text{m}^3$  layer over the last decade (Figures 2a, 3c, and 3d).

In the Indian Ocean, a strong positive trend is observed between the  $26.2$ - and  $26.8\text{-kg}/\text{m}^3$  isopycnal layers (Figures 3e and 3f). This warming is compensated by a comparable loss of  $1.8 \times 10^{22} \text{ J}$  within the denser layers ( $\sigma_\theta = 26.8$ – $27.0 \text{ kg}/\text{m}^3$ ; Figures 3e and 3f). This suggests a possible heat convergence in the SAMW, which could also be associated with a lightening of the SAMW above  $26.8 \text{ kg}/\text{m}^3$ , while underlying loses heat (below  $26.8 \text{ kg}/\text{m}^3$ ). Note also that the tropical Indian Ocean waters ( $\sigma_\theta < 24.0 \text{ kg}/\text{m}^3$ ) strongly warmed during the last decade (Figures 3e and 3f). This upper tropical Indian warming trend is to be balanced with the strong upper tropical Pacific cooling ( $\sigma_\theta < 24.0 \text{ kg}/\text{m}^3$ ; Figures 3h and 3j) observed over the same period. This balance results from upper ocean heat exchange between tropical Pacific and Indian Oceans through the Indonesian throughflow over the period after 2003 (Lee et al., 2015).

Although the North Pacific Ocean shows slight warming (less  $0.5 \times 10^{22} \text{ J}$ ; Figure 3i) around the  $25.5\text{-kg}/\text{m}^3$  isopycnal layer, in the South Pacific Ocean, high decadal variability is observed for two distinct water masses. First, around the  $25.5\text{-kg}/\text{m}^3$  isopycnal layer that is mainly related to the South Pacific Eastern STMW (SPEATMW; Roemmich & Cornuelle, 1998, Wong & Johnson, 2003). The OHC shows a large increase ( $1 \times$

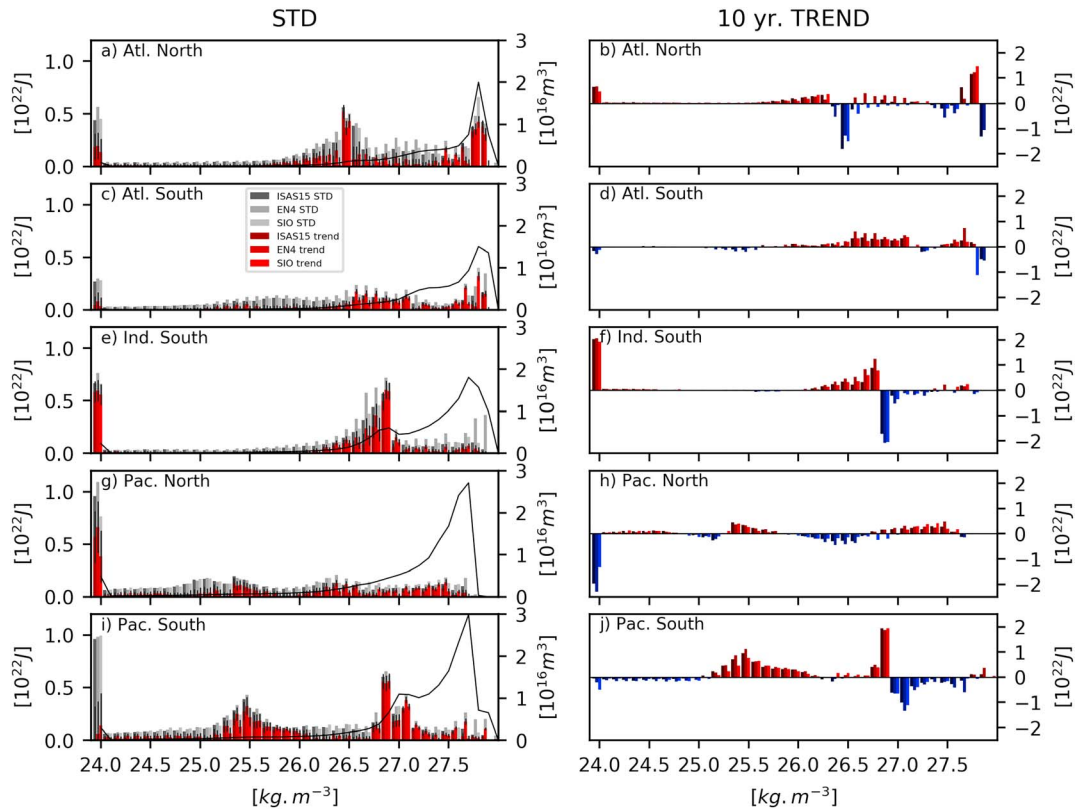


**Figure 3.** (left panels) Interannual STD (removing the monthly climatologies) of OHC change for every  $0.1\text{-kg/m}^3$  isopycnal layer between  $24.0$  and  $27.5\text{ kg/m}^3$  (gray), part of the STD explained by the trend over the 2006–2015 period (reds), uncertainty on trend (error bars), and the mean volume of each isopycnal layer (thin black line). (right panels) Heat trend gain (red) and loss (blue) over the 2006–2015 period computed from the ISAS15 (dark red/blue), SIO (light red/blue), and EN4 (red/blue) over the period 2006–2015 in (a and b) North Atlantic, (c and d) South Atlantic, (e and f) Indian, (g and h) North Pacific, and (i and j) South Pacific basins. The layer within surface and  $24\text{ kg/m}^3$  is computed as a unique layer.

$10^{22}\text{ J}$ ) mainly explained by the 10-year trend (Figures 3i and 3j). Second, in the South Pacific, the SAMW presents a large heat gain ( $2 \times 10^{22}\text{ J}$ ) within the  $\sigma_\theta = 26.7\text{--}26.9\text{ kg/m}^3$  isopycnal layer, compensated by an equivalent loss within the underlying Antarctic Intermediate Water (AAIW) at  $\sigma_\theta = 26.9\text{--}27.3\text{ kg/m}^3$  (Figures 3i and 3j).

In order to better characterize and localize the water masses affected by the strong 10-year trend, Figures 4 and 5 show the map of the thickness mean and STD, OHC decadal trends computed from ISAS and from individual profiles, temperature trend, and thickness trend for some key isopycnal layers. Figure 4 shows the core of STMW ( $\sigma_\theta = 25.4\text{--}25.5$  and  $\sigma_\theta = 26.4\text{--}26.5\text{ kg/m}^3$ ), and Figure 5 shows the SAMW density range ( $\sigma_\theta = 26.7\text{--}26.8$ ,  $\sigma_\theta = 26.8\text{--}26.9$ , and  $\sigma_\theta = 26.9\text{--}27.0\text{ kg/m}^3$  from left to right). The computation of OHC from both the ISAS product and individual profiles provide consistent trend patterns (with a confidence level at 95%).

The largest isopycnal layer thickness, that is, low stratification (Figures 4a, 4f, 5a, 5f, and 5k), is consistent with the location of MW pools as described in Hanawa and Tally (2001). As suggested by Figure 1, the strongest OHC trends are observed in SPESTMW (Figures 4a–4c) and NASTMW (Figures 4f–4h). The SPESTMW shows a noticeable warming trend ( $+2\text{ W/m}^2$ ; Figure 4b) within  $\sigma_\theta = 25.4\text{--}25.5\text{ kg/m}^3$ , coincident with the increase of the water mass thickness (Figure 4e) and temperature trend (Figure 4d). In the North Atlantic, within the isopycnal layer between  $\sigma_\theta = 26.4\text{--}26.5\text{ kg/m}^3$  becomes thinner (Figure 4f), which is consistent with the heat loss trend within the NASTMW ( $-4\text{ W/m}^2$ ; Figure 4g).

In the Southern Hemisphere, the strongest OHC signals are observed within the isopycnal layer range of SAMW (Figure 5). Within the  $\sigma_\theta = 26.7\text{--}26.8\text{ kg/m}^3$  isopycnal layer (Figure 5a), OHC change shows the strongest positive trend, up to  $+10\text{ W/m}^2$ , localized south of Australia from west of the Australian Great

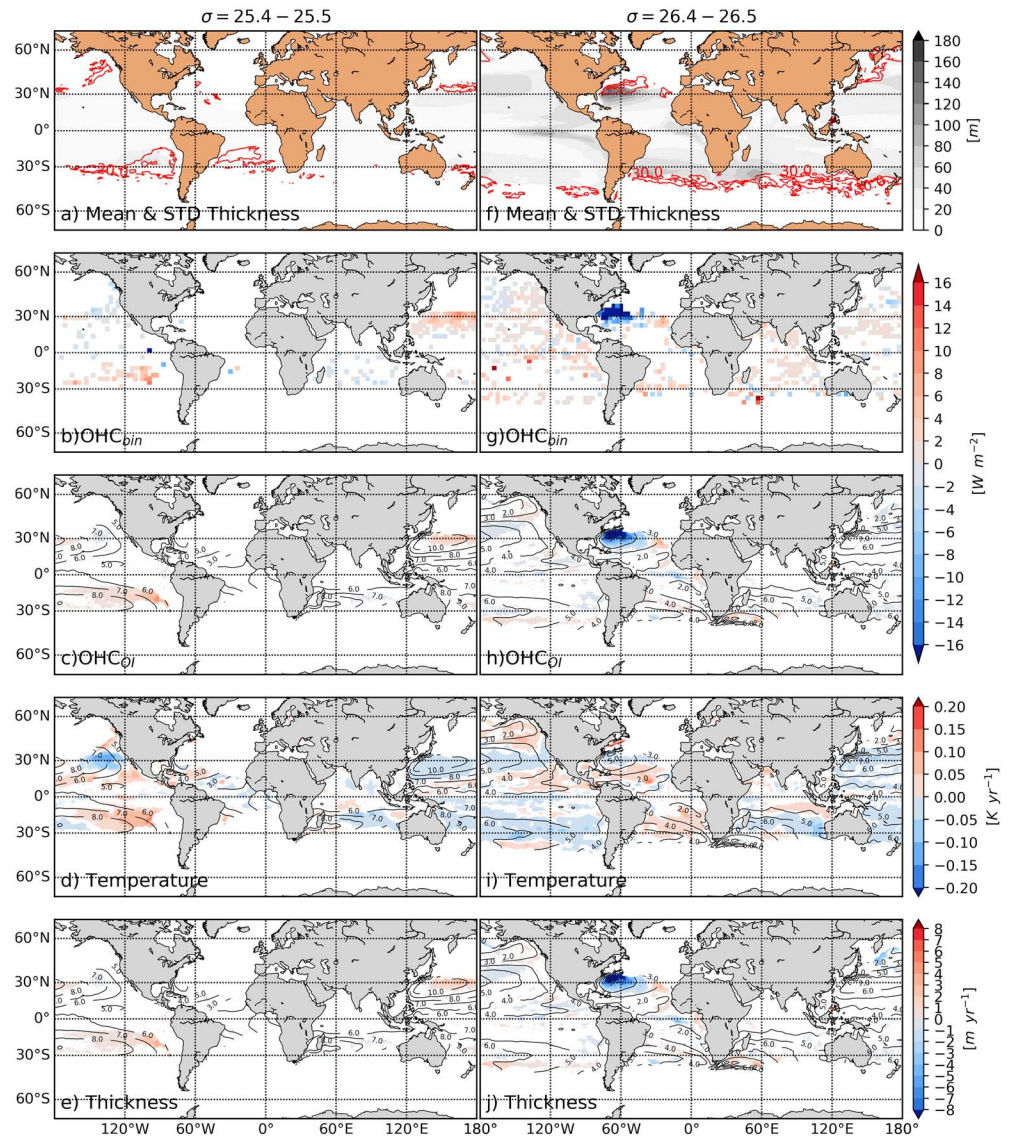


**Figure 4.** Global isopycnal decomposition of the Subtropical Mode Water (STMW) for (left column)  $\sigma_{\theta} = 25.4\text{--}25.5$  and (right column)  $\sigma_{\theta} = 26.4\text{--}26.5$  kg/m<sup>3</sup> isopycnal layers. (a and f) Mean and interannual STD of thickness (m), (b and g) OHC<sub>bin</sub> trend over the 2006–2015 period from ISAS15 (W/m<sup>2</sup>), (c and h) OHC<sub>OI</sub> over 2006–2015 period from individual profiles (W/m<sup>2</sup>; only trends significant with a confidence level at 95% as been plotted), (d and i) averaged layer temperature trend (K/year), and (e and j) thickness trend (m/year). Blanked area indicates that the isopycnal layer does not permanently exist in this area.

Bight to the southern tip of New Zealand (Figures 5b and 5c), corresponding to the southeastern Indian SAMW (SEISAMW; McCarthy & Talley, 1999; Figure 5a). In contrast, the south subtropical Indian Ocean exhibits a strong heat loss (around  $-9$  W/m<sup>2</sup>; Figures 5b and 5c). This negative OHC trend is associated with a comparable horizontal pattern of isopycnal layer thickness loss (Figures 5d and 5e). The  $\sigma_{\theta} = 26.8\text{--}26.9$  kg/m<sup>3</sup> isopycnal layer experiences a heat loss of about  $-7$  W/m<sup>2</sup> localized in the eastern South Indian Ocean subtropics and Australian Great Bight within the SEISAMW (Figures 5f–5h). For the southern Pacific Ocean, positive heat trend of  $+9$  W/m<sup>2</sup> is observed between  $180\text{--}110^{\circ}\text{W}$  and  $35\text{--}50^{\circ}\text{S}$ , also explained by the associated thickness change of the isopycnal layer (Figures 5g–5j). For the southern Pacific, the densest water masses shown in Figures 5k–5o within the  $\sigma_{\theta} = 26.9\text{--}27.0$  kg/m<sup>3</sup> isopycnal layer (Figure 5k) lost  $-6$  W/m<sup>2</sup> during the 10-year period, consistently with the shrinking of the isopycnal layer, while in the southeast Pacific the same layer shows thicken and warming trends around  $+2\text{--}4$  W/m<sup>2</sup> between  $120\text{--}90^{\circ}\text{W}$  and  $40\text{--}60^{\circ}\text{S}$  (Figures 5j–5l).

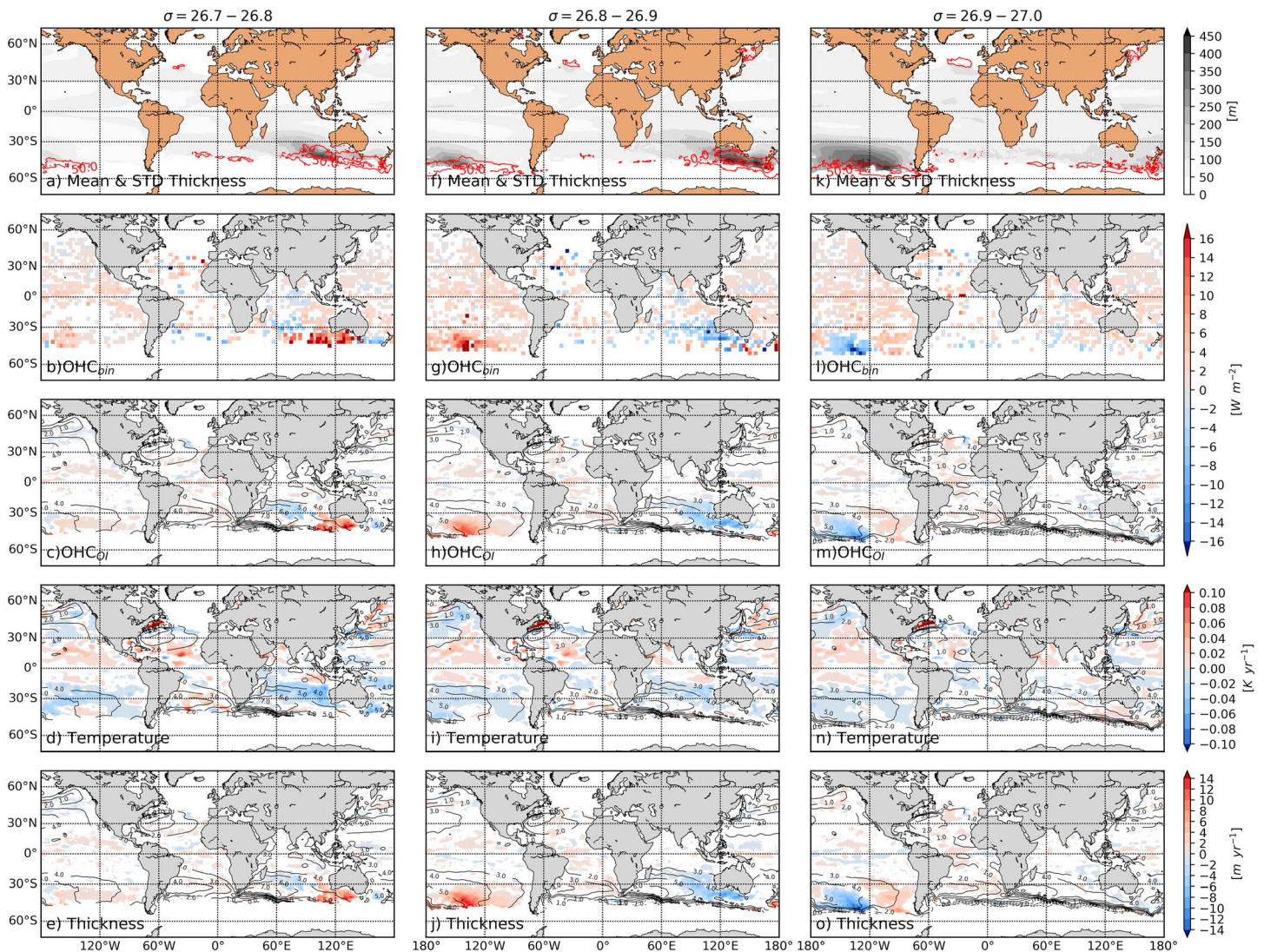


Figure 5. Same as Figure 4 except for density ranges of SAMW masses: (a–e)  $\sigma_\theta = 26.7\text{--}26.8$ , (f–j)  $\sigma_\theta = 26.8\text{--}26.9$ , and (k–o)  $\sigma_\theta = 26.9\text{--}27.0$ .

Note that the North Atlantic Madeira Mode Water (Siedler et al., 1987) also shows contraction and is associated with a heat loss ( $-2\text{ W/m}^2$ ; Figure 4e), while slight warming signature is associated with the North Atlantic Subpolar Mode Water ( $+2\text{ W/m}^2$ ; Figures 5k–5o).

### 3.2. Interannual Variability

#### 3.2.1. SPESTMW

As suggested by the difference between the total interannual variability and the STD associated to the 10-year trend (Figure 3), the volume trend does not explain the entire interannual variability to 2006–2015 trend. In order to better characterize the spatiotemporal patterns of interannual water mass variability, yearly thickness anomalies (averaged over one year starting from September to next September) between September 2006 and September 2015 have been mapped along the isopycnal layer corresponding to the SPESTMW ( $\sigma_\theta = 25.4\text{--}25.5\text{ kg/m}^3$ ; Figure 6). This layer has experienced a water mass subduction during the late austral winter (during September) off the South American coast around  $25^\circ\text{S}$  ( $110^\circ\text{--}90^\circ\text{W}/30^\circ\text{--}10^\circ\text{S}$  box; Figure 6; Wong & Johnson, 2003; Sato & Suga, 2009; Kolodziejczyk & Gaillard, 2013). The subduction operates in the region of late winter deepest mixed layer (in September, Figure 6; gray contours), that is, where the buoyancy loss is the strongest during austral winter and the mean Ekman pumping is negative (Kolodziejczyk & Gaillard, 2013). Year-to-year subduction anomalies modify the thickness (i.e., OHC) of

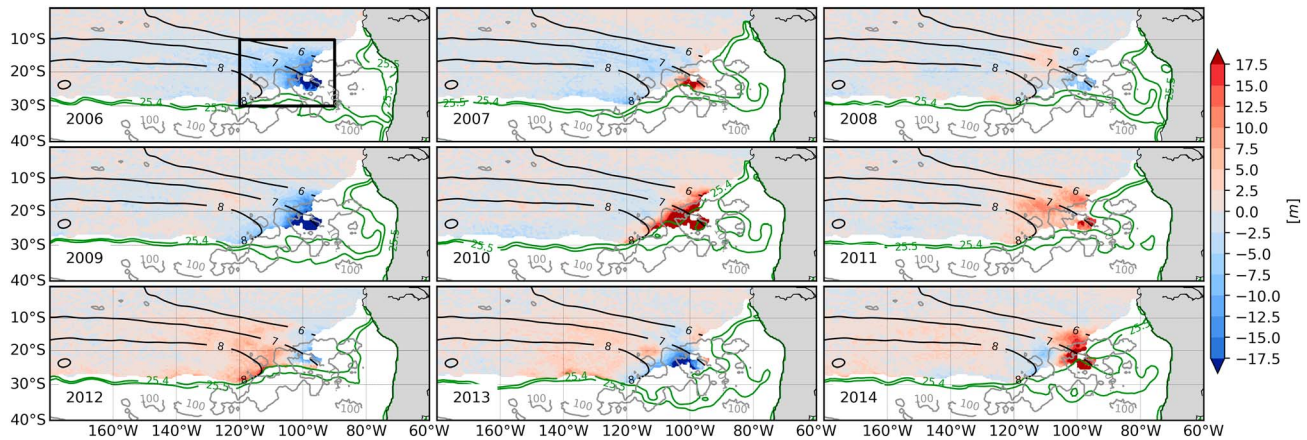


**Figure 6.** South-Eastern Subtropical Pacific: interannual thickness anomaly (in m) within the  $\sigma_{\theta} = 25.4\text{--}25.5 \text{ kg/m}^3$  isopycnal layer between 2006 and 2015 for the Southern Hemisphere (year averaged between September and the following August) from ISAS15. Black contours are the Montgomery stream functions (in  $\text{m}^2/\text{s}^2$ ) on the  $\sigma_{\theta} = 25.5 \text{ kg/m}^3$  isopycnal surface which is an approximate estimate of the geostrophic current streamlines. Green contours are the September position of the outcrops of the  $\sigma_{\theta} = 25.4\text{--}25.5 \text{ kg/m}^3$  isopycnal layer. Gray contours denote the mean September mixed layer depth (in m) computed from ISAS15 with a  $0.03\text{-kg/m}^3$  criterion. Black box in 2006 limits the subduction area within  $120^{\circ}\text{--}90^{\circ}\text{W}/30^{\circ}\text{--}10^{\circ}\text{S}$ .

SPESTMW. Then, the thickness anomalies are propagated westward following the subtropical gyre circulation (Figure 6, solid black lines; Kolodziejczyk & Gaillard, 2012). In September 2006, 2009, and 2013 negative volume anomalies are subducted in the subtropical south-eastern Pacific, while in September 2010, 2011, and 2014 strong thickness positive anomalies are generated (Figure 6). It is worth noticing, however, that the strong amplitude of the thickness anomaly shows a rapid westward decrease following the Montgomery streamlines (black contours; Figure 6;  $7\text{--}8 \text{ m}^2/\text{s}^2$ ) from the subduction region. During September, the outcrop latitudinal position of  $\sigma_{\theta} = 25.4\text{--}25.5 \text{ kg/m}^3$  (Figure 6; green contours) are qualitatively correlated with the thickness anomalies: during 2006, 2009, and 2013, the outcrop position of the  $\sigma_{\theta} = 25.4 \text{ kg/m}^3$  isopycnal is located further southward and the outcrop area of the  $\sigma_{\theta} = 25.4\text{--}25.5 \text{ kg/m}^3$  layer is smaller than during late winter 2010, 2011, and 2014. This suggests that the greater buoyancy loss during winter may be responsible for the larger generation of SPESTMW water mass (Kolodziejczyk & Gaillard, 2012, 2013; Nonaka & Sasaki, 2007; Schneider et al., 1999).

OHC, thickness, and temperature anomalies (Figures 7a, 7c, and 7e) in the first 1,000 km from the subduction area are well correlated with the mixed layer depth interannual anomalies (gray bar; Figures 7a, 7c, and 7e). As shown by Kolodziejczyk and Gaillard (2012, 2013), this suggests the dominant role of the interannual variability of late winter buoyancy loss. During the largest event of positive anomalies (2010–2011), enhanced downward Ekman pumping seems to contribute to the injection of volume and temperature anomalies in the interior of the ocean (Figures 7a, 7c, and 7e). Furthermore, in the subtropical south eastern Pacific, the El Niño–Southern Oscillation (ENSO) variability is clearly correlated to the detrended SPESTMW interannual variability, especially during the 2009–2010 ENSO event (Figures 7a, 7c, and 7e; Wong & Johnson, 2003; Kolodziejczyk & Gaillard, 2012).

From the subduction region clear westward propagation of OHC, thickness, and mean temperature anomalies are visible (Figures 7b, 7d, and 7f) with alternative negative (2006, 2009, and 2013) and positive (2010, 2011, and 2014) anomalies. These OHC, thickness, and temperature anomalies propagate at a speed close to the mean current velocities, around  $0.05 \text{ m/s}$  (solid black line; Figures 7b, 7d, and 7e). The mean speed of propagation of thickness and temperature anomalies has been estimated with a lagged correlation  $0.056 \pm 0.001$  and  $0.062 \pm 0.001 \text{ m/s}$ , which is very close to the mean current velocity. OHC interannual variability is mainly explained by the isopycnal thickness variability. OHC and thickness anomaly propagation are closely related each other (correlation of  $r = 0.99$ ; significant at 95%). In other hand, OHC and temperature anomaly correlation is weaker ( $r = 0.49$ ). Westward of  $120^{\circ}\text{W}$ , clearly the volume anomalies vanish (Figure 7d). It can be explained by diapycnal and isopycnal mixing/diffusion (e.g., Abernathey et al., 2016; Cerovecki et al., 2013; Downes et al., 2011; Speer & Tzipermann, 1992; Speer & Forget, 2013; Tzipermann, 1986; Walin, 1982).

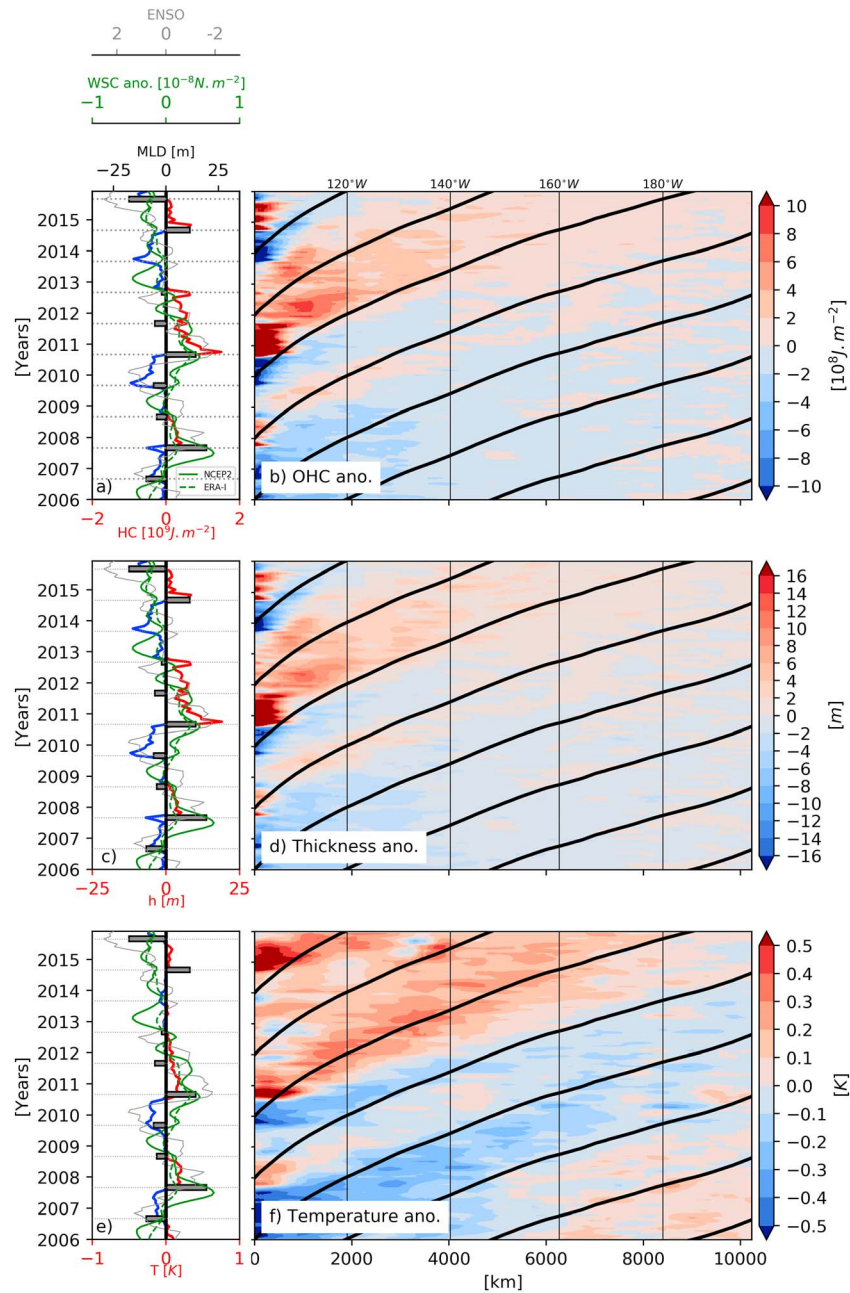


**Figure 7.** (a) Detrended Interannual OHC anomaly (in J/m<sup>2</sup>), (c) thickness anomaly (in m), and (e) temperature anomaly (in K) within the  $\sigma_\theta = 25.4\text{--}25.5$  kg/m<sup>3</sup> isopycnal layer between 2006 and 2015 (colors) computed for the black box in Figure 6. For each of these panels, we have overlaid the ENSO index (gray), wind stress curl anomaly (in N/m<sup>2</sup>) computed from NCEP2 (solid green) and ERA-INTERIM (dashed green), and August–September mixed layer depth anomaly (in m; gray bars). Distance–time diagrams (b) OHC, (d) thickness, and (f) temperature anomalies (with the 2006–2015 trend) computed along ( $\pm 5^\circ$  distance) 7.5-m<sup>2</sup>/s<sup>2</sup> Montgomery stream function on  $\sigma_\theta = 25.4\text{--}25.5$  kg/m<sup>3</sup> isopycnal layer between 2006 and 2015. Black curves are the streamline characteristics along the 7.5-m<sup>2</sup>/s<sup>2</sup> Montgomery stream function.

To further investigate the relationship between thickness and temperature anomaly propagation in the SPESTMW, the vertical structure of the isopycnal depth (colors; Figure 8) and isopycnal layer potential temperature (contours; Figure 8) annual anomalies were computed along 15°S between 2007 and 2015 (Figure 8). Within  $\sigma_\theta = 25.0\text{--}26.0$  kg/m<sup>3</sup> layer, westward propagation of alternative negative isopycnal temperature anomalies in 2007–2011 (Figures 8a–8e) and positive anomalies in 2012–2014 (Figures 8f–8i) are observed. The westward propagation of negative (positive) temperature anomalies are also associated with

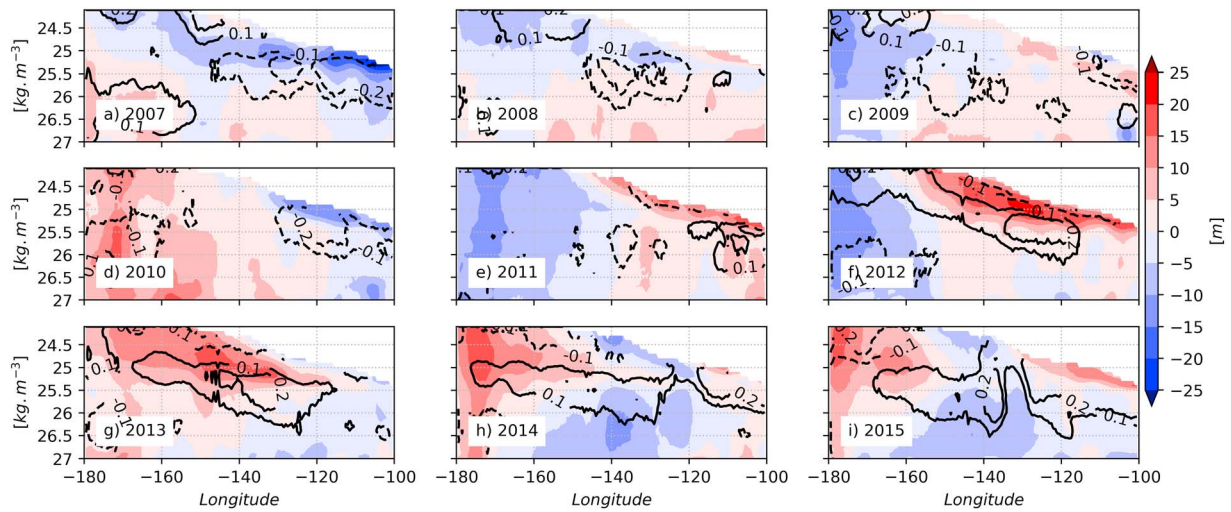


**Figure 8.** The  $\sigma_\theta$ -longitude section of  $\sigma_\theta$  depth anomalies (in m) and isopycnal layer temperature anomaly (in K) along  $15^\circ\text{S}$  in the subtropical South Pacific over 2007–2015. Green contours are the September position of the outcrops of the  $\sigma_\theta = 26.8\text{--}26.9\text{ kg/m}^3$  isopycnal layer in the Northern Hemisphere (Southern Hemisphere). Gray contours denote the mean September mixed layer depth (in m) computed from ISAS15 with a  $0.03\text{-kg/m}^3$  criterion.

positive (negative) isopycnal depth anomalies below  $\sigma_\theta = 25.5\text{ kg/m}^3$  and negative (positive) anomalies above  $\sigma_\theta = 25.5\text{ kg/m}^3$ , as for instance, in 2008 (2014). This vertical structure of the isopycnal depth suggests high baroclinic vertical modes with sign opposed to the isopycnal heaving over the vertical associated with for the propagation of such thickness anomalies around  $\sigma_\theta = 25.5\text{ kg/m}^3$ . However, Figure 8 does not exhibit a clear vertical position of the zeros crossing for the actual isopycnal vertical displacement anomalies. For example, in 2008–2009 the zero crossing displacement is located around  $25.5\text{ kg/m}^3$ , while in 2012–2013, the zero crossing is deeper, around  $26.5\text{ kg/m}^3$ . The short time series and depth span limitation (2,000-m depth) of the Argo data set prevent us to further speculate on the baroclinic structure of the interannual signal.

Nevertheless, the westward propagation speed of the second linear baroclinic free mode of long Rossby waves ( $\sim 0.01\text{--}0.04\text{ m/s}$ ; blue; Figure 9) is slightly too slow to explain such a propagation close to the baroclinic mean speed. One potential explanation could be the advective dynamic mode as reported in an isopycnal model

study by Liu and Shin (1999). This mode is a key feature of interior subtropical gyre adjustment under thermodynamic forcing, that is, buoyancy flux (Liu, 1999). To compare the velocity of such a mode with the theoretical velocity of the advective second baroclinic mode, the barotropic flow speed (black dashed line; Figure 9) was overlaid on the theoretical long planetary linear Rossby wave group speed. The order of magnitude of the advective mode speed (barotropic + second mode speed; Figure 9) was close to the OHC and thickness anomaly propagation speed (dashed-dotted line; Figure 9), as suggested by Liu and Shin (1999).

### 3.2.2. South Pacific SAMW

In the southern central Pacific ( $170\text{--}120^\circ\text{W}$ ), the South Pacific SAMW (SPSAMW) is located within the  $26.8\text{--}26.9\text{-kg/m}^3$  isopycnals. This region has been reported a hot spot of subduction around  $140^\circ\text{W}$  (Sallée et al., 2010). During 2006–2010 (2011–2015), this isopycnal layer exhibits negative (positive) thickness anomalies (Figures 10a and 10b) and a negative (positive) anomaly of OHC (contours) and depth (colors; Figures 10c and 10d). This is explained by the vertical shallowing (deepening) of the isopycnals which is amplified around the  $26.9\text{-kg/m}^3$  isopycnal (Figures 10c and 10d). This result implies

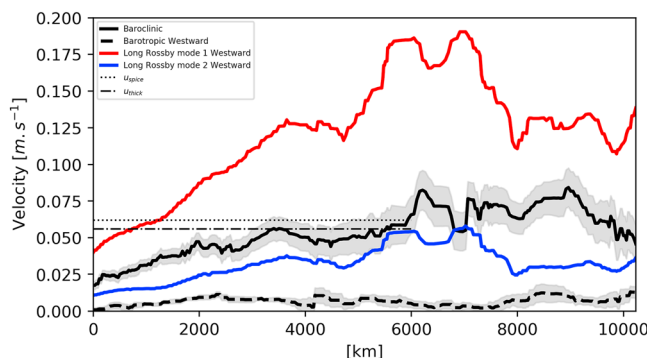


**Figure 9.**  $U_{\text{spice}}$  (dotted line) and  $u_{\text{thick}}$  (dashed-dotted line) are the averaged propagation velocity computed from the lag correlation of temperature and thickness anomalies in Figure 7, respectively. Baroclinic velocity (solid black): westward barotropic velocity (dashed black), westward first (red), and second (blue) speed of long Rossby waves ( $C_n = \beta \lambda_n^2$ , where  $C_n$  is the wave speed of the  $n$ th baroclinic mode of long Rossby waves, radius  $\beta$  is the meridional gradient of the Coriolis parameter, and  $\lambda_n$  is the Rossby radius associated with the  $n$ th baroclinic mode) along a  $7.5\text{ m}^2/\text{s}^2$  Montgomery stream function (in m/s).

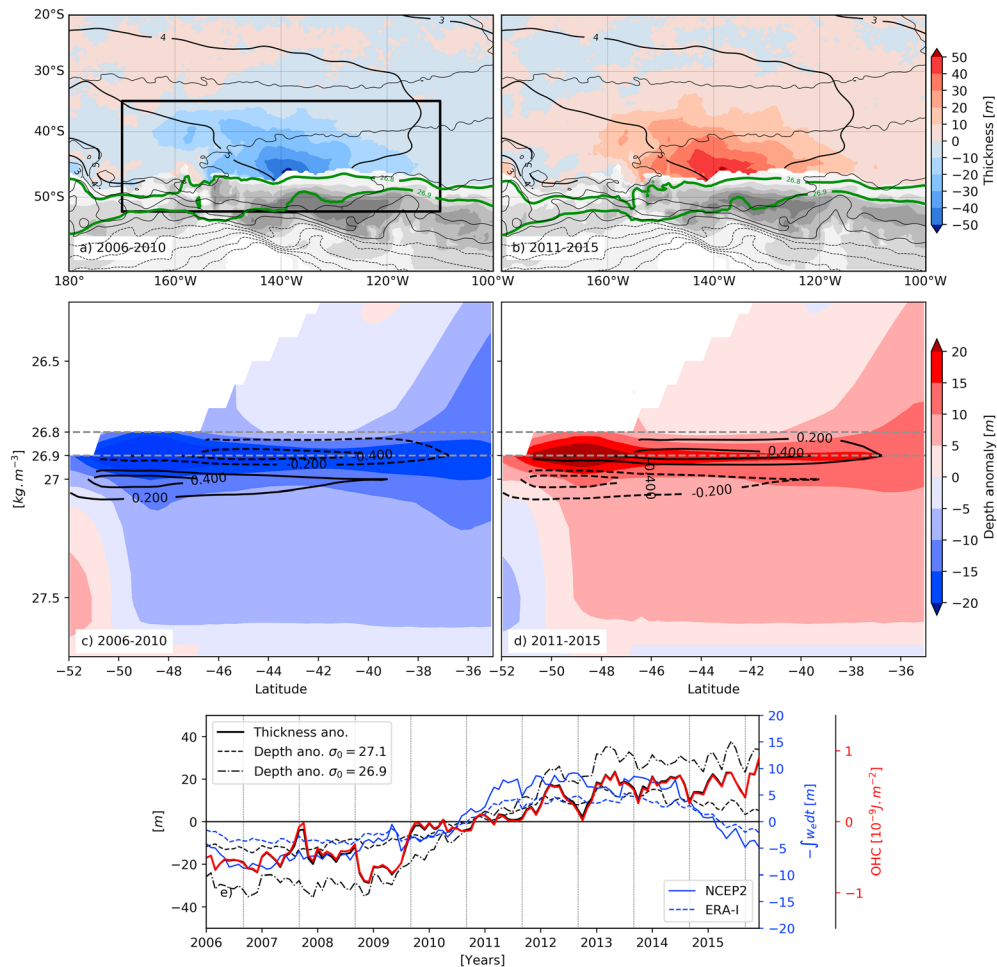


**Figure 10.** (a) The 2006–2010 and (b) 2011–2015 averaged thickness interannual anomaly within the  $\sigma_\theta = 26.8\text{--}26.9 \text{ kg/m}^3$  isopycnal layer in the south central Pacific (in m). Green contours are the September position of the outcrops of the  $\sigma_\theta = 26.8\text{--}26.9 \text{ kg/m}^3$  isopycnal layer. Gray shading denote the September mixed layer depth (in m; C.I. = 100 m) computed from ISAS15 with a  $0.03\text{-kg/m}^3$  criterion. Black box in (a) limits the subduction area within  $170^\circ\text{--}110^\circ\text{W}/52^\circ\text{--}35^\circ\text{S}$ . Black contours are the Montgomery stream functions (in  $\text{m}^2/\text{s}^2$ ) on the  $\sigma_\theta = 26.9 \text{ kg/m}^3$  isopycnal surface which is an approximate estimate of the geostrophic current streamlines. Thin black contour (solid and dashed) is the absolute dynamic topographic from Aviso averaged over the 2006–2015 period (C.I. = 0.2 m, solid being positive). (c) The 2006–2010 and (d) 2011–2015 zonal average (in the black box) of isopycnal depth anomalies (in m; shading) and isopycnal layer OHC anomalies (in  $\text{J/m}^2$ ; contours). (e) Thickness (solid black) and OHC (solid red) anomalies of the  $\sigma_\theta = 26.8\text{--}26.9 \text{ kg/m}^3$  isopycnal layer and depth anomalies of isopycnals (dashed and dotted black), time-integrated Ekman pumping anomaly (with respect to the 2006–2015 period; in m) computed from NCEP (solid blue) and ERA-INTERIM (dashed blue), and September mixed layer depth anomalies from ISAS15 with a  $0.03\text{-kg/m}^3$  criterion (gray bar; in m). Computed within  $170^\circ\text{--}110^\circ\text{W}/52^\circ\text{--}35^\circ\text{S}$ .

that the SPSAMW volume increase is mechanically associated with volume decrease of the underlying water masses due to the downward maximum excursion around  $\sigma_\theta = 26.9 \text{ kg/m}^3$ .

The potential role of the wind stress curl forcing and Ekman pumping on the observed isopycnal heaving are investigated in the southern Pacific Ocean along with the time evolution of the  $26.9\text{-}$  and  $27.1\text{-kg/m}^3$  isopycnals (Figure 10e). Over the period 2006–2009, the time-integrated Ekman pumping anomaly is consistent with the relative stability of the isopycnal depth (Figure 10e). In contrast, between 2009 and 2012, the Ekman pumping (Figure 10e) are consistent with the  $\sigma_\theta = 26.9 \text{ kg/m}^3$  and  $\sigma_\theta = 27.1 \text{ kg/m}^3$  isopycnals downward displacement (Figure 10e). Again, over 2012–2013, stable Ekman pumping is associated to a stable isopycnal depth, then drop again in 2014–2015. After 2013 only the  $27.1\text{-kg/m}^3$  isopycnal is compatible with the isopycnal shallowing suggested by the Ekman pumping. In contrast, after 2013, the  $26.9\text{-kg/m}^3$  isopycnal and layer thickness (and OHC) do not decrease. In the South Pacific, the qualitative agreement between isopycnal vertical displacement induced by Ekman pumping and observed isopycnal displacement is observed in the

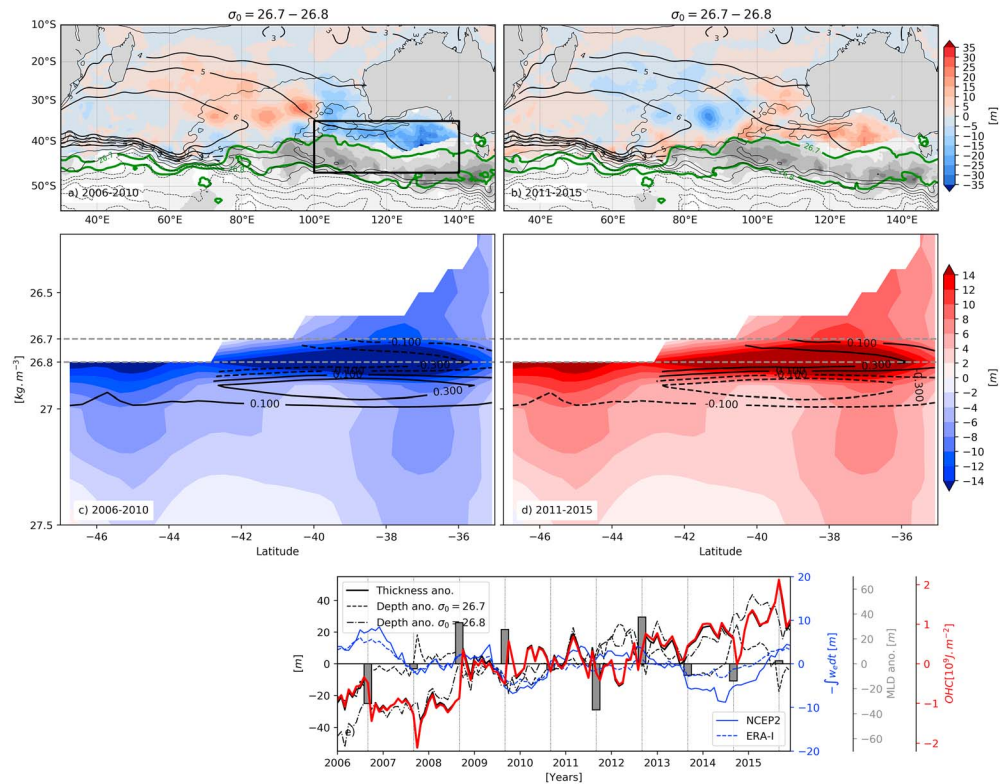


**Figure 11.** Same as in Figure 10 except for  $\sigma_{\theta} = 26.7\text{--}26.8 \text{ kg/m}^3$  isopycnal layer in the southern Indian Ocean.

SAMW lower isopycnal limits ( $\sigma_{\theta} = 27.1 \text{ kg/m}^3$ ) as suggested by Gao et al. (2017), but fails to explain the increase of depth, thickness, and OHC within the  $26.8\text{--}26.9\text{-kg/m}^3$  isopycnal layer. This suggests that the relation between the wind forcing and volume gain is not evident within  $26.8\text{--}26.9\text{-kg/m}^3$  layer. Water mass formation by the buoyancy flux could also explain such SAMW change as suggested by Abernathey et al. (2016). Eventually, as reported by Sallée et al. (2010), between  $150^{\circ}\text{W}$  and  $120^{\circ}\text{W}$  within  $26.8\text{--}26.9\text{-kg/m}^3$  isopycnal layer, subduction of water mass by induction could be responsible for the volume flux in the interior SAMW as suggested by the strong MLD gradient associated with northward flux Antarctic Circumpolar Current at surface (materialized by the ADT contours; Figures 10a and 10b).

### 3.2.3. South-Eastern Indian SAMW

Within the  $\sigma_{\theta} = 26.7\text{--}26.8 \text{ kg/m}^3$  layer, the SEISAMW (Figure 11) exhibits the strongest thickness anomaly in the south-eastern Indian Ocean around the Great Australian Bight (Figures 11a and 11b). In this range of density, this region has also been reported to be a hot spot of MW subduction (Sallée et al., 2010). In this region (black square in Figure 11a) over the period 2006–2010 negative thickness anomalies are observed with a subsequent positive anomaly between 2010 and 2015. Northwest from this region, along the mean streamline between  $4$  and  $6 \text{ m}^2/\text{s}^2$  (Figure 11, black contours) between Australia and Madagascar, the thickness anomalies have an opposite decadal evolution: positive during 2006–2010 and negative during 2010–2016 (Figures 11a and 11b). Zonal average of isopycnal depth anomalies across the subtropical Indian Ocean within  $47\text{--}35^{\circ}\text{S}/100\text{--}140^{\circ}\text{E}$ S (black square in Figure 11a) are shown in Figures 11c and 11d. Above  $\sigma_{\theta} = 26.8 \text{ kg/m}^3$ , OHC increases in the SAMW due to the strong deepening of isopycnal surface around  $\sigma_{\theta} = 26.8 \text{ kg/m}^3$ . The opposite behavior is found for the density layer below  $26.8 \text{ kg/m}^3$ .

Contrary to the SPSAMW, the deepening of  $\sigma_{\theta} = 26.8 \text{ kg/m}^3$  isopycnal surface (black dashed-dotted; Figure 11e) does not show agreement with the time-integrated Ekman pumping anomaly (blue curves; Figure 11e). The air-sea flux interaction may be a possible candidate. Therefore, we have investigated and diagnosed the late winter (September) mixed layer depth anomaly as a proxy of cumulated winter buoyancy flux. Between 2006 and 2013, the positive (negative) mixed layer depth anomalies are consistent with the

sudden increase (decrease) of thickness and OHC anomalies within the 26.7–26.8-kg/m<sup>3</sup> isopycnals (black and red solid lines; Figure 11e). However, after 2013, the OHC continues to rise but the MLD does not show strong variability. Even if the MLD variability seems to have some impact on the thickness and OHC of the SEISAMW, our results suggest that other mechanisms not addressed in this study or an interaction between different processes must have an important role to explain the SEISAMW volume change.

#### 4. Discussion and Conclusion

In this study, the OHC, thickness, and temperature along isopycnal layers were computed using three optimal interpolated products and individual Argo profiles. Isopycnal decomposition reveals a clear picture of global water mass interannual variability and the hot spots of the OHC change over the 2006–2015 period. As shown in previous studies, Southern Hemisphere MWs have stored the largest amount of heat along the global oceans (Desbruyères et al., 2017; Gao et al., 2017; Häkkinen et al., 2016; Roemmich et al., 2015) from the Earth's Energy Imbalance causing the actual planetary global warming (von Schuckmann et al., 2016). This study allows us to infer a more precise picture of the interannual OHC and water mass variability and their associated mechanisms.

The first important finding of this study is that only a few, well-localized water masses are responsible for the main global OHC change over 2016–2015, that is, the upper ocean MWs and intermediate waters (and tropical water in the Indian and Pacific Oceans; Lee et al., 2015). In the Southern Hemisphere, the strongest warming signals have been found for the SPESTMW and SAMW. Concerning the SPESTMW, the strongest OHC interannual to decadal increase signal was found within  $\sigma_{\theta} = 25.4\text{--}25.5\text{ kg/m}^3$ . The SAMW showed an important warming over the 2006–2015 period. The main OHC hot spots within the SAMW were located: (i) above  $\sigma_{\theta} = 26.8\text{ kg/m}^3$  in the southeastern Indian Ocean, which corresponds with the SEISAMW (McCarthy & Talley, 1999), and (ii) in the central south Pacific Ocean within the 26.8–26.9-kg/m<sup>3</sup> isopycnals (SPSAMW). These hot spots for ocean heat ventilation (Rintoul, 2018) are also consistent with an average mode water ventilation location identified by Sallée et al. (2010) by estimating the subduction rates. These three water masses alone are responsible for great part of the decadal OHC intake in Southern Hemisphere. Interestingly, over the last decade, the North Atlantic STMW, the so-called Eighteen Degree Mode Water, showed a strong OHC and volume decrease after 2010, as previously reported in literature (Evans et al., 2017; Häkkinen et al., 2015).

Second, at interannual time scale the OHC change is mainly explained by STMW and SAMW volume change associated with the isopycnal heaving, while vertical average temperature (i.e., spiciness) of the MW layers is weakly correlated with OHC change. In the Southern Hemisphere, it appears that the MW change is explained by a lightening of these water masses; that is, they are translating toward a lighter isopycnal range. This is consistent with a convergence of mass and heat from AAIW toward the SAMW for the Southern Hemisphere (e.g., Abernathy et al., 2016; Cerovecki et al., 2012; Downes et al., 2011). This is compatible with the previously observed heaving tendency of an upper ocean warming (Desbruyères et al., 2017; Häkkinen et al., 2016). However, at interannual time scale, this study suggests that the relationship between water mass volume change and isopycnal heaving is not straightforward and it depends of complex atmospheric forcing and dynamics.

Indeed, water mass interannual variability mechanisms were inferred in three key regions: the south-eastern Indian Ocean, the south Pacific, and the subtropical south-eastern Pacific. In the subtropical south-eastern Pacific, over 2006–2015, the SPESTMW generations are correlated with ENSO atmospheric variability (O'Kane, Matear, Chamberlain, & Oke, 2014; Wong & Johnson, 2003). In this region the ENSO atmospheric variability strongly impacts anomalous interannual buoyancy flux and Ekman pumping and consequently imprints interannual change of SPESTMW water masses (Kolodziejczyk & Gaillard, 2012, 2013; Nonaka & Sasaki, 2007).

Then, in the eastern subtropical South Pacific, the propagation of the anomalous spiciness and thickness signal were observed in the subtropical gyre at a speed close to that of the mean gyre circulation within the  $\sigma_{\theta} = 25.4\text{--}25.5\text{ kg/m}^3$  (Kolodziejczyk & Gaillard, 2012, 2013). The propagation of isopycnal thickness anomalies (i.e., a dynamic tracer) and spiciness anomalies (i.e., a passive tracer) is reported in the literature. Using an isopycnal model Liu (1999) and Liu and Shin (1999) studied the adjustment response of a subtropical gyre to

dynamical and thermodynamical forcing. They found that two kinds of response to thermodynamic forcing (i.e., buoyancy forcing) can be detected: (i) a dynamic mode associated with propagation of isopycnal depth anomalies and (ii) a passive mode associated with tracer propagation along the ventilation flow path. In the first case, the propagation speed and path are close to the mean ventilation flow and results from non-Doppler shifted wave modes, that is, advection of the second and higher baroclinic mode of long Rossby waves by the barotropic current.

Our results might suggest such a possible bimodal propagation, meaning that an active tracer propagation is dominant for the volume (mass) adjustment for the South Pacific Eastern Subtropical. The observed thickness propagation is too slow to be related to the first mode of baroclinic long Rossby wave propagation generally associated with gyre adjustment (Tailleux, 2006). This deviation from theory may be explained by topographic and mean baroclinic current effects, which modify the ambient PV gradient, thus either slowing down or speeding up the observed long Rossby waves (e.g., Colin de Verdière & Tailleux, 2005; Killworth & Blundell, 2003a, 2003b; Liu, 1999; Tailleux, 2006). Although in the theoretical gyre circulation Liu (1999) suggests that advective mode of active tracer speed ups the no-mean flow long Rossby wave, linear theory is close (but not necessary equal) to the velocity of the mean baroclinic current in the thermocline layer. In spite of large uncertainty in our velocity estimate (inherent to the integration of thermal wind balance from hydrologic data and altimetry), our results could suggest such a dynamic.

Another explanation could be the multiscale and nonlinear propagation of baroclinic disturbance associated with an unstable baroclinic mode (Hochet et al., 2015; O'Kane, Matear, Chamberlain, Oliver, & Holbrook, 2014; O'Kane et al., 2016). In subtropical regions, these baroclinic disturbances could be associated with an unstable mode of propagation. The propagation of dynamical and passive tracer observed in the SPESTMW are however not found in the same latitude as those of O'Kane, Matear, Chamberlain, Oliver, and Holbrook (2014). Ours are located around 15°S, while O'Kane, Matear, Chamberlain, & Oke, 2014, O'Kane, Matear, Chamberlain, Oliver, & Holbrook, 2014) baroclinic disturbance are found around 35°S. Small baroclinic disturbance are however visible in O'Kane, Matear, Chamberlain, Oliver, & Holbrook, 2014, their Figure 11) around 110°W and 20°S, which could correspond to our region of SEPSTMW formation. O'Kane, Matear, Chamberlain, & Oke, 2014, O'Kane, Matear, Chamberlain, Oliver, & Holbrook, 2014) have identified paths, so-called oceanic “storm tracks,” and speed comparable to long Rossby wave propagation, which are both largely in agreement with our observations.

Concerning the variability of SAMW, our results show that an important OHC and volume convergence took place between 2006 and 2015, while the waters in the underlying density layer cooled and reduced volume over the same period. This warming and expansion of the SAMW may be associated with water mass transformation by mixing and air-sea flux between the SAMW/AAIW (Abernathey et al., 2016; Downes et al., 2011; Evans et al., 2014; Sallée et al., 2010). For both the southern Indian and Pacific Oceans, climate models have shown that Ekman transport plays a dominant role in SAMW and AAIW ventilation/upwelling (Rintoul & England, 2002). Cross-isopycnal Ekman mass transport due to zonal wind along subtropical front is responsible for mass ventilation within the density class of SAMW. Air-sea flux-induced temperature and salinity changes are likely to be insignificant in the thick SAMW (Church et al., 1991; Rintoul & England, 2002; Warren, 1972). However, northward Ekman transport has been shown to be largely compensated by strong southward eddy-induced transport (Lumpkin & Speer, 2007; Sloyan & Rintoul, 2001). The MW volume change found here could be related to induction of water masses by the strong Antarctic Circumpolar Current meandering in interaction with topography, but the localized modality of transfer of water masses between the surface ML and the ocean interior remained to be clarified (Rintoul, 2018; Sallée et al., 2010). In the other hand, the SAMW volume change could be associated with larger-scale ocean adjustment processes involving isopycnal heaving at decadal time scale but the link between wind forcing and local water mass change remained to be explored (Gao et al., 2017).

In the South Pacific SAMW region, our results suggest that volume and OHC increase observed over the last decade are likely to be partly explained by interannual event of wind forcing change over the period 2009 and 2012. In the Southern Ocean, the intensity and meridional excursion of the eastward zonal wind is associated with the Southern Annular Mode oscillation (Marshall, 2003). This atmospheric interannual mode of variability may be responsible for strong change in the Ekman pumping and heat uptake change over the Southern Ocean region (Drijfhout et al., 2014).

In contrast, the South Eastern Indian SAMW decadal water mass formation is not clearly related to the wind stress curl change over the Argo period. We speculate a possible control by the air-sea buoyancy forcing changes reflected by the mixed layer depth during late winter. Cerovecki et al. (2013) suggest that a hot spot of water mass transformation by air-sea flux is located precisely in the SEISAMW region. They note also a significant interannual variability during 2005 and 2006 potentially responsible for the generation/destruction of SEISAMW via air-sea flux and interior diapycnal mixing. The SEISAMW are exported toward the South Pacific SAMW via the strong wind driven eastward Antarctic Circumpolar Current. This could help to rationalize the lack of correlation observed with the Ekman pumping and SEISAMW volume change. At a longer time scale in the Southern Ocean, in a climate model with increasing radiative forcing, a reduction of the volume of intermediate waters is also suggested, which is mostly redistributed to SAMW. At the same time, the poleward shift of the atmospheric jet is associated with an increase (decrease) of subtropical (intermediate) water outcrops (Downes et al., 2011; Meijers et al., 2012; Sallée et al., 2013). MW and intermediate water appear to play a key role in heat, freshwater, and carbon storage (Fine et al., 2017; Sallée et al., 2013; Séférian et al., 2012). A water mass formation/transformation approach based on observations might be useful to improve the assessment of the complete atmospheric/interior mixing control on interannual and local variability in upper ocean water masses.

The isopycnal layer OHC and water mass decomposition carried out in this study provided a better insight into the mechanisms at work in the water mass subduction and interannual interior property variability. Although the isopycnal decomposition from  $z$ -coordinate OI products may increase the error on location of interpolated isopycnal layer, the reasonable constancy between three independent (from methodological perspective) OI products of increasing vertical resolution as well as the use of individual profiles isopycnal decomposition provides more confidence in our results. Since the interannual time scale seems to be locally relevant to study the redistribution of water mass heat and freshwater in the upper ocean, further work is needed to better document and understand the mechanism associated with forcing, mixing, turbulence, and Rossby wave propagation at interannual time scale in more dynamically constant reanalysis and models. The sustained Argo floats network has proven its unprecedented capacity to address and investigate these questions.

#### Acknowledgments

Acknowledgements This work was supported by the AcCOLADE LEFE project and LOPS ISAS project. ISAS15 is produced at LOPS as part of the *Service National d'Observation Argo-France* and made freely available (doi: <http://doi.org/10.17882/52367>). William Llovel was supported by "Louis Gentil-Jacques Bourcart" fellowship from the French "Académie des Sciences" and by OVALIE project from ESA Living Planet Fellowship fundings. This work is mainly based on the Argo data set and thus benefited from the in-depth involvement of scientists and data managers with regard to float deployment and data validation and distribution (<http://www.argo.ucsd.edu/>). The altimeter products were produced by Ssalto/Duacs and distributed by Aviso, with support from CNES (<http://www.aviso.altimetry.fr/duacs/>). MDT\_CNES-CLS13 was produced by CLS Space Oceanography Division and distributed by Aviso, with support from CNES (<http://www.aviso.altimetry.fr/>). N.K. thanks Pr. Alain Colin de Verdière for many valuable and helpful discussions and providing the barotropic current computation. The authors also thank anonymous reviewers that greatly helped to improve the manuscript.

#### References

- Abernathy, R. P., Cerovecki, I., Holland, P. R., Newsom, E., Mazloff, M., & Talley, L. D. (2016). Water-mass transformation by sea ice in the upper branch of the Southern Ocean overturning. *Nature Geoscience*, *9*(8), 596–601. <https://doi.org/10.1038/NGeo2749>
- Abraham, J. P., Baringer, M., Bindoff, N. L., Boyer, T., Cheng, L. J., Church, J. A., et al. (2013). A review of global ocean temperature observations: Implications for ocean heat content estimates and climate change. *Reviews of Geophysics*, *51*, 450–483. <https://doi.org/10.1002/rog.20022>
- Bretherton, F., Davis, R., & Fandry, C. (1976). Technique for objective analysis and design of oceanographic experiment applied to MODE-73. *Deep Sea Research and Oceanographic Abstracts*, *23*(7), 559–582. [https://doi.org/10.1016/0011-7471\(76\)90001-2](https://doi.org/10.1016/0011-7471(76)90001-2)
- Cerovecki, I., Talley, L. D., Mazloff, M. R., & Maze, G. (2013). Subantarctic Mode Water formation, destruction, and export in the eddy-permitting Southern Ocean State Estimate. *Journal of Physical Oceanography*, *43*(7), 1485–1511. <https://doi.org/10.1175/JPO-D-12-0121.1>
- Church, J. A., White, N. J., Konikow, L. F., Domingues, C. M., Cogley, J. G., Rignot, E., et al. (1991). Revisiting the Earth's sea-level and energy budget from 1961 to 2008. *Geophysical Research Letters*, *38*(18). <https://doi.org/10.1029/2011GL048794>
- Colin de Verdière, A., & Tailleux, R. (2005). The interaction of a baroclinic mean flow with long Rossby waves. *Journal of Physical Oceanography*, *35*(5), 865–879. <https://doi.org/10.1175/JPO2712.1>
- De Boyer Montégut, C., Madec, G., Fisher, A. S., Lazar, A., & Iudicone, D. (2004). Mixed layer depth over the global ocean: An examination of profile data and a profile-based climatology. *Journal of Geophysical Research*, *109*, C12003. <https://doi.org/10.1029/2004JC002378>
- Desbruyères, D., McDonagh, E. L., King, B. A., & Thierry, V. (2017). Global and full-depth ocean temperature trends during the early twenty-first century from Argo and repeat hydrography. *Journal of Climate*, *30*(6), 1985–1997. <https://doi.org/10.1175/JCLI-D-16-0396.1>
- Döös, K., Nilsson, J., Nycander, J., & Brodeau, L. (2012). The world ocean thermohaline circulation. *Journal of Physical Oceanography*, *42*(9), 1445–1460. <https://doi.org/10.1175/JPO-D-11-0163.1>
- Downes, S. M., Gnanadesikan, A., Griffies, S. M., & Sarmiento, J. L. (2011). Water mass exchange in the Southern Ocean in coupled climate model. *Journal of Physical Oceanography*, *41*(9), 1756–1771. <https://doi.org/10.1175/2011JPO4586.1>
- Drijfhout, S. S., Blaker, A. T., Josey, S. A., Nurser, A. J. G., Sinha, B., & Balmaseda, M. A. (2014). Surface warming hiatus caused by increased heat uptake across multiple ocean basins. *Geophysical Research Letters*, *41*, 7868–7874. <https://doi.org/10.1002/2014GL061456>
- Durack, P. J., Glecker, P. J., Landerer, F. W., & Taylor, K. E. (2014). Quantifying underestimates of long-term upper-ocean warming. *Nature Climate Change*, *4*(11), 999–1005. <https://doi.org/10.1038/nclimate2389>
- Evans, D. G., Toole, J., Forget, G., Zika, J. D., Naveira Garabto, A. C., Nurser, A. J. G., & Yu, L. (2017). Recent wind-driven variability in Atlantic water mass distribution and meridional overturning circulation. *Journal of Physical Oceanography*, *47*(3), 633–647. <https://doi.org/10.1175/JPO-D-16-0089.1>
- Evans, D. G., Zika, J. D., Garabato, A. C. N., & Nurser, A. J. G. (2014). The imprint of Southern Ocean overturning on seasonal water mass variability in Drake Passage. *Journal of Geophysical Research: Oceans*, *119*, 7987–8010. <https://doi.org/10.1002/2014JC010097>

- Fine, R. A., Peacock, S., Maltrud, M. E., & Bryan, F. O. (2017). A new look at ocean ventilation time scales and their uncertainties. *Journal of Geophysical Research: Oceans*, *122*, 3771–3798. <https://doi.org/10.1002/2016JC012529>
- Forget, G., Maze, G., Buckley, M., & Marshall, J. (2011). Estimated seasonal cycle of North Atlantic Eighteen Degree Water Volume. *Journal of Physical Oceanography*, *40*, 1201–1221.
- Gaillard, F., Autret, E., Thierry, V., Galaup, P., Coatanoan, C., & Loubrieu, T. (2009). Quality control of large Argo data sets. *Journal of Atmospheric and Oceanic Technology*, *26*(2), 337–351. <https://doi.org/10.1175/2008JTECHO552.1>
- Gaillard, F., Reynaud, T., Thierry, V., Kolodziejczyk, N., & von Schuckman, K. (2016). ISAS-13 re-analysis: Climatology and inter-annual variability deduced from Global Ocean Observing Systems. *Journal of Climate*, *29*(4), 1305–1323. <https://doi.org/10.1175/JCLI-D-15-0028.1>
- Gao, L., Rintoul, S. R., & Yu, W. (2017). Recent wind-driven change in Subantarctic Mode Water and its impact on ocean heat storage. *Nature Climate Change*, *31*.
- Good, S. A., Martin, M. J., & Rayner, N. A. (2013). EN4: Quality controlled ocean temperature and salinity profiles and monthly objective analyses with uncertainty estimates. *Journal of Geophysical Research: Oceans*, *118*, 6704–6716. <https://doi.org/10.1002/2013JC009067>
- Gould, J., Roemmich, D., Wijffels, S., Freeland, H., Ignaszewsky, M., Jianping, X., et al. (2004). Argo profiling floats bring new era of in situ ocean observations. *Eos, Transactions of the American Geophysical Union*, *85*(19), 185–191. <https://doi.org/10.1029/2004EO190002>
- Häkkinen, S., Rhines, P. B., & Worthen, D. L. (2015). Heat content variability in the North Atlantic Ocean in ocean reanalyses. *Geophysical Research Letters*, *42*, 2901–2909. <https://doi.org/10.1002/2015GL063299>
- Häkkinen, S., Rhines, P. B., & Worthen, D. L. (2016). Warming of the global ocean: Spatial structure and water mass trends. *Journal of Climate*, *29*(13), 4949–4963. <https://doi.org/10.1175/JCLI-D-15-0607.1>
- Hanawa, K., & Tally, L. (2001). Modes Waters. In G. Siedler & J. Church (Eds.), *Ocean circulation and climate, chapter mode waters, International Geophysics Series* (pp. 373–386). New York: Academic Press.
- Hochet, A., Huck, T., & Colin de Verdière, A. (2015). Large-scale baroclinic instability of the mean oceanic circulation: A local approach. *Journal of Physical Oceanography*, *45*(11), 2738–2754. <https://doi.org/10.1175/JPO-D-15-0084.1>
- IPCC (2013). Climate Change 2013: The Physical Science Basis. In T. F. Stocker, D. Qin, G.-K. Plattner, M. Tignor, S. K. Allen, J. Boschung, A. Nauels, Y. Xia, V. Bex, & P. M. Midgley (Eds.), *Contribution of Working Group I to the Fifth Assessment Report of the Intergovernmental Panel on Climate Change*, (p. 1535). Cambridge, United Kingdom and New York, NY, USA: Cambridge University Press. <https://doi.org/10.1017/CBO9781107415324>
- Killworth, P. D., & Blundell, J. R. (2003a). Long extratropical planetary wave propagation in the presence of slowly varying mean flow and bottom topography. Part I: The local problem. *Journal of Physical Oceanography*, *33*(4), 784–801. [https://doi.org/10.1175/1520-0485\(2003\)33<784:LEPWPI>2.0.CO;2](https://doi.org/10.1175/1520-0485(2003)33<784:LEPWPI>2.0.CO;2)
- Killworth, P. D., & Blundell, J. R. (2003b). Long extratropical planetary wave propagation in the presence of slowly varying mean flow and bottom topography. Part II: Ray propagation and comparison with observations. *Journal of Physical Oceanography*, *33*(4), 802–821. [https://doi.org/10.1175/1520-0485\(2003\)33<802:LEPWPI>2.0.CO;2](https://doi.org/10.1175/1520-0485(2003)33<802:LEPWPI>2.0.CO;2)
- Kolodziejczyk, N., & Gaillard, F. (2012). Observation of spiciness inter-annual variability in the Pacific pycnocline. *Journal of Geophysical Research-Oceans*, *117*, C12018. <https://doi.org/10.1029/2012JC008365>
- Kolodziejczyk, N., & Gaillard, F. (2013). Variability of the heat and salt budget in the subtropical south-eastern Pacific mixed layer between 2004 and 2010: Spice injection mechanism. *Journal of Physical Oceanography*, *43*(9), 1880–1898. <https://doi.org/10.1175/JPO-D-13-04.1>
- Kolodziejczyk, N., A. Prigent-Mazella, F. Gaillard (2017). ISAS-15 temperature and salinity gridded fields. SEANO. <http://doi.org/10.17882/52367>
- Kolodziejczyk, N., Reverdin, G., Gaillard, F., & Lazar, A. (2014). Low-frequency thermohaline variability in the Subtropical South Atlantic pycnocline during 2002–2013. *Geophysical Research Letters*, *41*, 6468–6475. <https://doi.org/10.1002/2014GL061160>
- Lee, S.-K., Park, W., Baringer, M. O., Gordon, A. L., Huber, B., & Liu, Y. (2015). Pacific origin of the abrupt increase in Indian Ocean heat content during the warming hiatus. *Nature Geoscience*, *8*(6), 445–449. <https://doi.org/10.1038/NGEO2438>
- Liu, Z. (1999). Forced planetary wave response in a thermocline gyre. *Journal of Physical Oceanography*, *29*(5), 1036–1055. [https://doi.org/10.1175/1520-0485\(1999\)029<1036:FPWRIA>2.0.CO;2](https://doi.org/10.1175/1520-0485(1999)029<1036:FPWRIA>2.0.CO;2)
- Liu, Z., & Shin, S.-I. (1999). On the thermocline ventilation of active and passive tracers. *Geophysical Research Letters*, *26*(3), 357–360. <https://doi.org/10.1029/1998GL900315>
- Llovel, W., & Terray, L. (2016). Observed southern upper-ocean warming over 2005–2014 and associated mechanisms. *Environmental Research Letters*, *11*, 124023(12). <https://doi.org/10.1088/1748-9326/11/12/124023>
- Lumpkin, R., & Speer, K. (2007). Global ocean meridional overturning. *Journal of Physical Oceanography*, *37*(10), 2550–2562. <https://doi.org/10.1175/JPO3130.1>
- Luyten, J. R., Pedlosky, J., & Stommel, H. (1983). The ventilated thermocline. *Journal of Physical Oceanography*, *13*(2), 292–309. [https://doi.org/10.1175/1520-0485\(1983\)013<0292:TVT>2.0.CO;2](https://doi.org/10.1175/1520-0485(1983)013<0292:TVT>2.0.CO;2)
- Marshall, G. J. (2003). Trends in the Southern Annular Mode from observations and reanalyses. *Journal of Climate*, *16*, 4134–4143.
- Maze, G., & Marshall, J. (2011). Diagnosing the observed seasonal cycle of Atlantic Subtropical Mode Water using potential vorticity and its attendant theorems. *Journal of Physical Oceanography*, *41*(10), 1986–1999. <https://doi.org/10.1175/2011JPO4576.1>
- McCarthy, M. C., & Talley, L. D. (1999). Three-dimensional isoneutral potential vorticity structure in the Indian Ocean. *Journal of Geophysical Research*, *104*(C6), 13,251–13,267. <https://doi.org/10.1029/1999JC900028>
- McCartney, M. S. (1977). In M. Angel (Ed.), *Subantarctic Mode Water. A voyage of Discovery* (pp. 103–119). Tarrytown, N.Y.: Pergamon Press.
- McCartney, M. S. (1982). The subtropical recirculation of mode waters. *Journal of Marine Research*, *40*, 427–464.
- McDougall, T. J., & Klocker, A. (2010). An approximate geostrophic streamfunction for use in density surface. *Ocean Modelling*, *32*(3-4), 105–117. <https://doi.org/10.1016/j.ocemod.2009.10.006>
- McDougall, T. J., & Kzysik, O. A. (2015). Spiciness. *Journal of Marine Research*, *73*(5), 141–152. <https://doi.org/10.1357/002224015816665589>
- Meijers, A. J. S., Shuckburgh, E., Bruneau, N., Sallée, J. B., Bracegirdle, T. J., & Wang, Z. (2012). Representation of the Antarctic Circumpolar Current in the CMIP5 climate models and future changes under warming scenarios. *Journal of Geophysical Research*, *117*, C12008. <https://doi.org/10.1029/2012JC008412>
- Nonaka, M., & Sasaki, H. (2007). Formation Mechanism for isopycnal temperature-salinity anomalies propagating from the eastern South Pacific to the equatorial region. *Journal of Climate*, *20*(7), 1305–1315. <https://doi.org/10.1175/JCLI4065.1>
- O’Kane, T. J., Matear, R. J., Chamberlain, M. A., & Oke, P. R. (2014). ENSO regimes and the late 1970’s climate shift: The role of synoptic weather and South Pacific ocean spiciness. *Journal of Computational Physics*, *271*, 19–38. <https://doi.org/10.1016/j.jcp.2013.10.058>

- O'Kane, T. J., Matear, R. J., Chamberlain, M. A., Oliver, E. C. J., & Holbrook, N. J. (2014). Storm tracks in the Southern Hemisphere subtropical oceans. *Journal of Geophysical Research: Oceans*, *119*, 6078–6100. <https://doi.org/10.1002/2014JC009990>
- O'Kane, T. J., Monselesan, D. P., & Maes, C. (2016). On the stability and spatiotemporal variance distribution of salinity in the upper ocean. *Journal of Geophysical Research: Oceans*, *121*, 4128–4148. <https://doi.org/10.1002/2015JC011523>
- Ollitrault, M., & Colin de Verdière, A. (2014). The ocean general circulation near 1000-m depth. *Journal of Physical Oceanography*, *44*(1), 384–409. <https://doi.org/10.1175/JPO-D-13-030.1>
- Rintoul, S. R. (2018). The global influence of localized dynamics in the Southern Ocean. *Nature*, *558*(7709), 209–218. <https://doi.org/10.1038/s41586-018-0182-3>
- Rintoul, S. R., & England, M. H. (2002). Ekman transport dominates local air–sea fluxes in driving variability of Subantarctic Mode Water. *Journal of Physical Oceanography*, *32*(5), 1308–1321. [https://doi.org/10.1175/1520-0485\(2002\)032<1308:ETDLAS>2.0.CO;2](https://doi.org/10.1175/1520-0485(2002)032<1308:ETDLAS>2.0.CO;2)
- Rio, M. H., Guinehut, S., & Larnicol, G. (2011). New CNES-CLS09 global mean dynamic topography computed from the combination of GRACE data, altimetry, and in situ measurements. *Journal of Geophysical Research*, *116*, C07018. <https://doi.org/10.1029/2010JC006505>
- Roemmich, D., Church, J., Gilson, J., Monselesan, D., Sutton, P., & Wijffels, S. (2015). Unabated planetary warming and its ocean structure since 2006. *Nature Climate Change*, *5*(3), 240–245. <https://doi.org/10.1038/nclimate2513>
- Roemmich, D., & Cornuelle, B. (1998). The Subtropical Mode Waters of the South Pacific Ocean. *Journal of Physical Oceanography*, *22*, 1178–1187.
- Roemmich, D., & Gilson, J. (2009). The 2004–2008 mean and annual cycle of temperature, salinity, and steric height in the global ocean from the Argo Program. *Progress in Oceanography*, *82*(2), 81–100. <https://doi.org/10.1016/j.pocean.2009.03.004>
- Sallée, J. B., Shuckburgh, E., Bruneau, N., Meijers, A. J. S., Bracegirdle, T. J., Wang, Z., & Roy, T. (2013). Assessment of Southern Ocean water mass circulation and characteristics in CMIP5 models: Historical bias and forcing response. *Journal of Geophysical Research: Oceans*, *118*, 1830–1844. <https://doi.org/10.1002/jgrc.20135>
- Sallée, J. B., Speer, K., Rintoul, S. R., & Wijffels, S. (2010). Southern Ocean thermocline ventilation. *Journal of Physical Oceanography*, *40*(3), 509–529. <https://doi.org/10.1175/2009JPO4291.1>
- Sasaki, Y. N., Schneider, N., Maximenko, N., & Lebedev, K. (2010). Observational evidence for propagation of decadal spiciness anomalies in the North Pacific. *Geophysical Research Letters*, *37*, L07708. <https://doi.org/10.1029/2010GL04716>
- Sato, K., & Suga, T. (2009). Structure and modification of the South Pacific Eastern Subtropical Mode Water. *Journal of Physical Oceanography*, *39*(7), 1700–1714. <https://doi.org/10.1175/2008JPO3940.1>
- Schneider, N. (2000). A decadal spiciness mode in the tropics. *Geophysical Research Letters*, *27*(2), 257–260. <https://doi.org/10.1029/1999GL002348>
- Schneider, N., Miller, A. J., Alexander, M. A., & Deser, C. (1999). Subduction of decadal North Pacific temperature anomalies: Observations and dynamics. *Journal of Physical Oceanography*, *29*(5), 1056–1070. [https://doi.org/10.1175/1520-0485\(1999\)029<1056:SODNPT>2.0.CO;2](https://doi.org/10.1175/1520-0485(1999)029<1056:SODNPT>2.0.CO;2)
- Séférian, R., Iudicone, D., Bopp, L., Roy, T., & Madec, G. (2012). Watermass analysis of effect of climate change on air–sea CO<sub>2</sub> fluxes: The Southern Ocean. *Journal of Climate*, *25*(11), 3894–3908. <https://doi.org/10.1175/JCLI-D-11-00291.1>
- Siedler, G., Kuhl, A., & Zenk, W. (1987). The madeira mode water. *Journal of Physical Oceanography*, *17*(10), 1561–1570. [https://doi.org/10.1175/1520-0485\(1987\)017<1561:TMMW>2.0.CO;2](https://doi.org/10.1175/1520-0485(1987)017<1561:TMMW>2.0.CO;2)
- Sloyan, B. M., & Rintoul, S. R. (2001). Circulation, renewal, and modification of Antarctic Mode and Intermediate Water. *Journal of Physical Oceanography*, *31*(4), 1005–1030. [https://doi.org/10.1175/1520-0485\(2001\)031<1005:CRAMOIA>2.0.CO;2](https://doi.org/10.1175/1520-0485(2001)031<1005:CRAMOIA>2.0.CO;2)
- Speer, K., & Forget, G. (2013). Global distribution and formation of mode waters. *International Geophysics*, *103*, 211–226. <https://doi.org/10.1016/B978-0-12-391851-2.00009-X>
- Speer, K., & Tzipermann, E. (1992). Rate of water mass formation in the North Atlantic Ocean. *Journal of Physical Oceanography*, *22*(1), 93–104. [https://doi.org/10.1175/1520-0485\(1992\)022<0093:ROWMFI>2.0.CO;2](https://doi.org/10.1175/1520-0485(1992)022<0093:ROWMFI>2.0.CO;2)
- Tailleux, R. (2006). The quasi-nondispersive regimes of long extratropical baroclinic Rossby waves over (slowly varying) topography. *Journal of Physical Oceanography*, *36*(1), 104–121. <https://doi.org/10.1175/JPO2823.1>
- Tzipermann, E. (1986). On the role of interior mixing and air–sea fluxes in determining the stratification and circulation of the ocean. *Journal of Physical Oceanography*, *16*(4), 680–693. [https://doi.org/10.1175/1520-0485\(1986\)016<0680:OTROIM>2.0.CO;2](https://doi.org/10.1175/1520-0485(1986)016<0680:OTROIM>2.0.CO;2)
- von Schuckmann, K., Palmer, M. D., Trenberth, K. E., Cazenave, A., Chambers, D., Champollion, N., et al. (2016). An imperative to monitor Earth's energy imbalance. *Nature Climate Change*, *6*(2), 138–144. <https://doi.org/10.1038/nclimate2876>
- Walín, G. (1982). On the relation between sea–surface heat flow and thermal circulation in the ocean. *Tellus*, *34*, 187–195.
- Warren, B. A. (1972). Insensitivity of subtropical mode water characteristics to meteorological fluctuations. *Deep Sea Research and Oceanographic Abstracts*, *19*(1), 1–19. [https://doi.org/10.1016/0011-7471\(72\)90069-1](https://doi.org/10.1016/0011-7471(72)90069-1)
- Wijffels, S., Roemmich, D., Monselesan, D., Church, J., & Gilson, J. (2016). Ocean temperatures chronicle the ongoing warming of Earth. *Nature Climate Change*, *6*(2), 116–118. <https://doi.org/10.1038/nclimate2924>
- Wong, A. P. S., & Johnson, G. C. (2003). South Pacific Eastern Subtropical Mode Water. *Journal of Physical Oceanography*, *33*(7), 1493–1509. [https://doi.org/10.1175/1520-0485\(2003\)033<1493:SPESMW>2.0.CO;2](https://doi.org/10.1175/1520-0485(2003)033<1493:SPESMW>2.0.CO;2)
- Worthington, L. V. (1959). The 18° Water in the Sargasso Sea. *Deep Sea Research*, *5*, 297–305.
- Zika, J. D., Sloyan, B. M., & McDougall, T. J. (2009). Diagnosing the Southern Ocean overturning from tracer fields. *Journal of Physical Oceanography*, *39*(11), 2926–2940. <https://doi.org/10.1175/2009JPO4052.1>